AGU ADVANCING EARTH AND SPACE SCIENCES

Water Resources Research®

RESEARCH ARTICLE

10.1029/2025WR041934

A Numerical Study of the Effects of Density Contrast on Flow, Turbulence, and Mixing at the Negro/Solimoes Confluence, Brazil

C. Jiang[1,2], M. Koken[3], G. Constantinescu[4], and C. Gualtieri[5]

[1]Water Conservancy Development Research Center of Taihu Basin Authority, Shanghai, China, [2]Key Laboratory of Hydrologic-cycle and Hydrodynamic System of Ministry of Water Resources, Hohai University, Nanjing, China, [3]Department of Civil Engineering, Middle East Technical University, Ankara, Turkey, [4]IIHR-Hydroscience and Engineering and Department of Civil and Environmental Engineering, The University of Iowa, Iowa City, IA, USA, [5]Department of Structures for Engineering and Architecture, University of Napoli Federico II, Napoli, Italy

Key Points:

- This is the first eddy resolving numerical investigation of flow and mixing at a large discharge and large aspect ratio confluence
- Density contrast affects spatial development of the mixing interface and the size and sense of rotation of the cells of secondary flow
- Differences and similarities are observed with respect to flow structures and mixing observed at medium and small size confluences

Correspondence to:

G. Constantinescu,
sconstan@engineering.uiowa.edu

Citation:

Jiang, C., Koken, M., Constantinescu, G., & Gualtieri, C. (2026). A numerical study of the effects of density contrast on flow, turbulence, and mixing at the Negro/Solimoes confluence, Brazil. *Water Resources Research*, *62*, e2025WR041934. https://doi.org/10.1029/2025WR041934

Received 11 AUG 2025
Accepted 12 APR 2026

Author Contributions:

Conceptualization: G. Constantinescu, C. Gualtieri
Data curation: C. Jiang
Formal analysis: C. Jiang, M. Koken, G. Constantinescu
Investigation: C. Jiang, M. Koken
Methodology: C. Jiang, M. Koken, G. Constantinescu
Resources: G. Constantinescu
Software: M. Koken, G. Constantinescu
Supervision: G. Constantinescu
Validation: C. Jiang, G. Constantinescu, C. Gualtieri
Writing – original draft: G. Constantinescu
Writing – review & editing: G. Constantinescu, C. Gualtieri

Abstract Eddy-resolving numerical simulations are conducted to investigate the effects of density contrast between the confluent flows on hydrodynamics, coherent structures and mixing downstream of the confluence between the Negro and Solimões Rivers, Brazil, which is characterized by both a large discharge (>100,000 m^3/s) and a large aspect-ratio ($W/D > 100$). The base case corresponds to real high-flow conditions observed at the confluence for which the density of the Negro River was smaller than that of the Solimões River and the ratio between the discharges in the Negro and Solimões rivers was $QR = Q_1/Q_2 = 0.32$. To be able to understand and isolate density contrast effects, numerical experiments are also conducted assuming negligible density effects between the incoming flows (i.e., with Richardson number $Ri = 0$) and with the densities reversed in the incoming streams. Despite the small density difference and very large discharges, a well-defined near-bed intrusion of heavier colder fluid develops in the $Ri > 0$ simulations and strongly affects the tilting of the mixing interface (MI) compared to the $Ri = 0$ case where despite the absence of streamwise-oriented vortical cells, the MI is strongly tilted toward the Negro River side of the main confluence channel. Moreover, the presence/absence of density contrast between the incoming streams affects the position, size and sense of rotation of the main helical cells of crossflow motions and the coherence of the vertical MI vortices.

1. Introduction

Confluences are integral and ubiquitous components of all natural drainage networks and riverine systems. Confluences play a critical role in regulating water, sediment, solutes and contaminants transport, as well as aquatic ecology (Rice et al., 2008), in streams and rivers (Constantinescu & Gualtieri, 2024). For example, how fast two streams of unequal temperature mix downstream of a confluence affects many ecological processes and is of great importance for river and reservoir management decisions (Arbat-Bofill et al., 2014; Marti-Cardona et al., 2016; Prats et al., 2010). The region characterized by converging flow streamlines, enhanced three-dimensionality of the flow, strong redistribution of the streamwise momentum and the presence of large-scale coherent structures generated by the confluence flows is generally referred to as the Confluence Hydrodynamic Zone (CHZ) (Kenworthy & Rhoads, 1995). At angled confluences, cells of secondary flow may be present, especially if regions of high bank curvature are present (Ashmore et al., 1992). The CHZ generally includes a zone of flow stagnation near the upstream junction corner, an area of flow deflection as the tributary enters the confluence and a mixing interface (MI) between the two converging flow. It is widely accepted that the CHZ hydro-morphodynamics and the rates of mixing are mainly affected by the planform geometry of the confluence, including regions of high bank curvature and the presence of floodplains in the tributaries (K. Li, Tang, Yuan, Xiao, et al., 2022; K. Li, Tang, Yuan, Xu, et al., 2022; Marinho et al., 2022; Riley et al., 2014; Souza De Morais et al., 2016; Sukhodolov & Sukhodolova, 2019; Yuan, Yan, et al., 2023), the momentum flux and discharge ratios of the tributaries, and by the level of concordance between the channel beds at the confluence entrance (Mosley, 1976; Guillen-Ludena et al., 2017). Large scale bathymetry features like scour holes can also affect the redistribution of streamwise momentum and the mixing rates in the main confluence channel (Gaudet & Roy, 1995). In addition, differences in the water density between the incoming tributary flows could affect flow and mixing due to flow stratification effects (e.g., see Ramòn et al., 2013, 2014; Lyubimova et al., 2014; Cheng & Constantinescu, 2018; Gualtieri et al., 2019; Pouchoulin et al., 2020).

During the last three decades, many theoretical, field, laboratory, numerical and remotely sensed image-based studies were carried out to identify and clarify hydro-sedimentary, morphodynamics and ecological processes at river confluences (Constantinescu & Gualtieri, 2024; Yuan et al., 2022). Despite significant progress, further research is needed at local scale to develop generalized theoretical hydrodynamics models (Sukhodolov et al., 2023) and to clarify the complex interaction among hydrodynamics, morphodynamics and ecological features (Gualtieri et al., 2017, 2020; Yuan, Qiu, et al., 2023), as well as large wood transport (Yuan, Zheng, et al., 2024), atmospheric reaeration (Shen et al., 2021; Yuan, Lin, et al., 2024) and the exchange between surface water and groundwater at river confluences (Lambs, 2004; Martone et al., 2020). At the basin scale, the multi-decadal changes in river connectivity associated with the evolution of confluences planform, as well as the effects of confluences on riverine network systems, need to be investigated.

Another still open issue is if the findings observed in laboratory-scale confluences and even in the field in small confluences do apply for large-scale confluences in terms of channel aspect ratios and/or large confluences characterized by large flow discharges, large flow depths and large aspect ratios. This is because large-scale confluences are likely to be characterized by a broader range of inflow conditions in terms of water chemistry, sediment concentration, and density of the tributary waters as large rivers can capture different geographic/topographic zones (Gualtieri et al., 2018; Lane et al., 2008). In addition, past studies of large-scale confluences have highlighted some differences in the mechanism responsible for the generation of secondary flow eddies (Lyubimova et al., 2020) and turbulent mixing processes (Bouchez et al., 2010). More specifically, it was suggested that the influence of secondary currents decreases at confluences with a large width-to-depth ratio (i.e., $W/D > 40$) due to the increased role of form roughness (Parsons et al., 2007; Szupiany et al., 2009). Furthermore, the study of Lane et al. (2008) of the large-scale confluence between Paranà and Paraguay rivers, Argentina, observed a striking change in the mixing rate under different flow conditions that was explained as being caused by turbulence-driven processes associated with the near-vertical shear layer (slow mixing) and turbulence-driven processes associated with the near-horizontal plane shear layer and channel-scale circulation as Paraguay flows under Paranà (rapid mixing). More recently, several field studies conducted from 2018 to 2021 at the large-scale ($W/D > 50$), moderate discharge confluence between the Yangtze River and the Poyang Lake in China found that hydrodynamics and mixing dynamics were controlled by the complex interactions among the momentum flux ratio, secondary flow and the lock-exchange flow associated with the density contrast between the two tributaries. Under low- and high-flow conditions, a single channel-scale cell of secondary flow and dual counter-rotating secondary cells promoted rapid and slow mixing, respectively (Li, Tang, Yuan, Xiao, et al., 2022; Xu et al., 2022; Yuan et al., 2021). Moreover, the numerical investigation conducted by Jiang et al. (2023) for the same confluence found no evidence of formation of streamwise-oriented vortical (SOV) cells, similar to those observed to form at small-scale confluences, despite the large confluence angle.

The large aspect ratio ($W/D > 100$) confluence between the Negro and Solimões rivers in the Amazon Basin ranks among the largest on Earth. Two field studies conducted during October 2014 and April/May 2015 identified some common hydrodynamics features noted in previous confluence studies and highlighted the entrainment at the riverbed of a plume of sediment-laden flow from the Solimões side to the Negro pool of the Amazon channel (Gualtieri et al., 2018; Ianniruberto et al., 2018; Trevethan et al., 2015). That sediment-laden flow has been first described by Laraque et al. (2009). In addition, the field studies found that the location and width of the MI were closely related to temporal changes of the discharge ratio between the tributaries. Furthermore, mixing between Negro and Solimões rivers was explained as a combination of four hydrologic and morphologic processes, such as difference in velocity and density between the rivers, bed friction and change in channel width. The differences in velocity and density were found to be the most important processes controlling mixing in the central part of the CHZ. Farther downstream, density contrast and bed friction had a comparable effect (Gualtieri et al., 2019). Despite these findings, the exact role of density contrast effects and how they interact with curvature effects induced by a region of high bank curvature as the Solimoes tributary connects with the main confluence channel are still to be clarified. The same is true for the main mixing mechanisms driven by the coherent structures generated inside the MI and around it (e.g., the eventual formation of SOV cells) and by cells of secondary flow. Also, not much is known on how these mixing mechanisms vary with increasing density contrast. These research gaps are likely also linked to the limitations inherent to field studies conducted at large confluences, such as the Negro/Solimões confluence, where extreme sampling conditions were observed especially at high flow conditions (i.e. transects lengths of up to 5.0 km, flow velocities up to 3 m/s, turbulent eddies larger than 40 m).

The use of eddy resolving simulations to investigate flow structure and mixing mechanisms at large river confluences has several advantages. The most important is related to the larger spatial resolution of the 3D data available from numerical simulations compared to field data. In particular, the spatial resolution of the transect velocity data collected in field experiments is not sufficient to resolve the flow inside the core of the SOV cells, if present. As such, data measured in the field at medium and large size confluences does not allow a full characterization of the size, position and dynamics of the large-scale coherent structures inside the CHZ. Field measurements trying to capture the dynamics of the vertical vortices inside the MI face similar limitations (Rhoads & Sukhodolov, 2001; Sukhodolov & Rhoads, 2001). Field data on mixing at large confluences is, in many cases, limited to information from videos of the free surface where differences in color and/or turbidity levels are used to visualize and characterize mixing. This is especially the case for high flow conditions, where measurements are difficult to conduct at large confluences because of hazard concerns. However, the mixing visualized at, or close to, the free surface is not always representative of subsurface patterns of mixing where additional mixing mechanisms may be present (e.g., vortices generated at the interface of near bed intrusions of heavier fluid with the lighter fluid above it, see Horna-Munoz et al., 2020). On the other hand, field measurements using acoustic Doppler current profiler (ADCP) profiling can only provide the distribution of the free-surface temperature along lines (i.e., the ADCP transects) and water sampling/multiparametric vertical profiling can yield only local measurements of temperature/water chemistry parameters at a limited number of ensembles within the channel cross-section.

In the present study, detached eddy simulations (DES) are conducted to investigate flow and turbulence structure at the Solimões/Negro confluence. Though such a numerical approach was previously used to perform similar investigations of flow, stratification effects and mixing at small size (e.g., Constantinescu, 2014; Constantinescu et al., 2011, 2012, 2014, 2016; Horna-Munoz et al., 2020) and medium size (e.g., Cheng & Constantinescu, 2018, 2020a; Jiang et al., 2023) natural confluences with concordant and discordant beds, this is the first study where eddy resolving simulations are used to study the physics of flow and transport processes at a large river confluence in terms of the discharges in the two tributaries and the channel aspect ratio. More specifically, previous field studies of the Negro/Solimões confluence have not fully clarified the complex dynamics of the MI. As such, the main objectives of the present study are to elucidate the role of density contrast between the incoming tributaries and bank-induced curvature in: (a) controlling the development of coherent structures inside and around the MI between the two streams and patterns of secondary flow; and (b) affecting the overall rate of mixing between the two rivers. To achieve these goals, and to better isolate the effects induced by density contrast between the tributary flows, the present study investigates and compares different scenarios in terms of the density difference between the Negro and Solimões rivers. Moreover, results are also compared with available experimental data collected in the field survey conducted during April/May 2015.

2. Study Area and Numerical Test Cases

The confluence of the Negro and Solimões Rivers is located near Manaus, in northern Brazil, where these rivers merge to form the Amazon River approximately 1,600 km upstream from its mouth on the Atlantic Ocean. This confluence has a junction angle of approximately 70° and is characterized by contrasting physical and chemical characteristics and sediment loads in the two rivers related to the different geology of the respective catchments in the Amazon Basin.

Two field surveys were carried out at this confluence (Figure 1) in both low (October 2014, FS-CNS1 campaign) and relatively high flow conditions (April/May 2015, FS-CNS2 campaign). During these campaigns, acoustic Doppler velocity profiling (ADCP), with a Teledyne RDI 600 kHz Rio Grande, and high-resolution seismic methods, such as echo-sounding and sub-bottom profiling, as well as a multi-parametric probe, were used. In total, 98 cross-sectional ADCP transects were collected, namely 50 in FS-CNS1 at 28 different locations and 48 in FS-CNS2 at 26 different locations. Furthermore, local temperature, pH, conductivity, turbidity, and total suspended sediment (TSS) concentration were measured over the water depth at several locations upstream and within the main confluence channel using an YSI EXO2 multi-parameter probe. More details on the two field surveys are given in Gualtieri et al. (2018, 2019) and Ianniruberto et al. (2018).

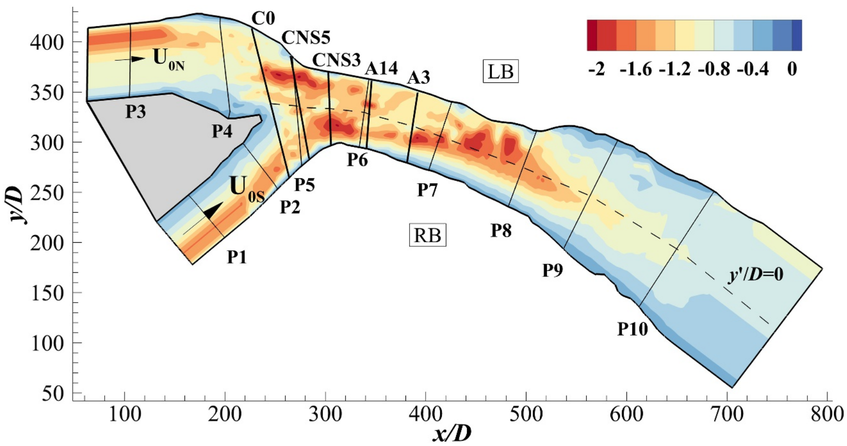

Figure 1. Horizontal view showing the confluence bathymetry and the cross sections where the solution is analyzed. The dashed black line passes through the points situated at mid distance between the right (right bank) and left (left bank) banks in the free surface plane. The contour levels show the bed elevation, z/D, where $D = 30$ m.

Table 1 lists the main flow properties and water characteristics of the Negro and Solimões rivers measured at the ADCP transects situated just upstream of the junction during the field surveys. Large differences in the discharge, flow velocity and direction between the two tributaries were present in the two field campaigns. Significant differences in the TSS concentration were also observed as the basin of the Solimões River (2,150,000 Km^2) includes the Eastern margin of the Andes, where large slopes and erodible rocks promote a high rate of sediment production. Meanwhile, the basin of the Negro River (687,000 Km^2) drains the Western slopes of the Guyana Shield, which is characterized by gentle gradients and densely vegetated margin, which results in low sediment production (Filizola et al., 2009). Water density was mainly driven by water temperature, but it was then adjusted using the TTS concentration as secondary factor. The equation proposed by Ford and Johnson (1983), already used in the study at the Ebro/Segre confluence (Ramón et al., 2013), was applied:

$$\Delta\rho_{\mathrm{TSS}} = \mathrm{TSS}\left(1 - \frac{1}{\mathrm{SG}}\right)10^{-3} \tag{1}$$

where SG is the specific gravity of suspended solids, assumed to be equal to 2.65. The adjustment led to an increase in the water density of Solimões River in the order of 10^{-2} kg/m^3. Table 1 also lists the relative density difference $\Delta\rho$ for the field surveys. The momentum flux, discharge and velocity ratios in Table 1 are calculated as the ratio between the corresponding variables in the Negro and Solimões rivers (i.e., discharge ratio $\mathrm{QR} = Q_N/Q_S$, where the subscript "N" refers to the Negro River and the subscript "S" refers to the Solimões River).

Iannirubert0 et al. (2018) identified a rocky bed with fine sand cover on the Negro side of confluence, a mid-channel peak/bar of apparent sedimentary origin about the MI and a bed consisting predominantly of coarser

Table 1
Main Flow and Geometrical Variables and Water Characteristics of the Negro and Solimões Rivers During the Two Field Campaigns

Field campaign	River	Q (m^3/s)	W (m)	D_{med} (m)	U_0 (m/s)	T (°C)	TSS (mg/L)	ρ (kg/m^3)	$\Delta\rho$ (kg/m^3)	QR	VR	MR
FS−CNS1	Negro	24,510	2,830	24.4	0.37	30.3	8.3	995.50	0.32	0.39	0.26	0.10
	Solimões	63,380	1,589	27.2	1.42	29.6	185.3	995.82				
FS−CNS2	Negro	33,501	2,875	31.3	0.37	29.0	4.1	995.90	0.36	0.32	0.22	0.07
	Solimões	105,205	1,925	28.6	1.65	28.0	108.6	996.26				

Note. Also included are the density difference between the two streams, the discharge ratio, the velocity ratio and the momentum flux ratio. Q = discharge; W = channel width; D_{med} = median depth; U_0 = average velocity in the cross section (Q/A); T = water temperature; TSS = total suspended sediments concentration; ρ = water density (based on water temperature and TSS concentration); $\Delta\rho$ = density difference between the two tributaries; QR = discharge ratio; VR = velocity ratio; MR = momentum flux ratio.

materials sediments on the Solimões side of confluence. Nordin et al. (1977) estimated a median diameter, d_{50}, of 0.977 mm (coarse sand) around the confluence.

The bathymetry (Figure 1) and flow parameters in the base case, DF, are based on the FS-CNS2 Survey (Gualtieri et al., 2019). The volumetric discharge was Q_S = 105,205 m^3/s for the Solimões River tributary and Q_N = 33,501 m^3/s for the Negro River tributary, which corresponded to a discharge ratio QR = 0.32 (Table 1). The mean streamwise velocities in the two tributaries were $U_{0N} = 0.37$ m/s and $U_{0S} = 1.65$ m/s, corresponding to a velocity ratio VR= U_{0N}/U_{0S} = 0.22. The momentum ratio MR = $\rho_N U_{0N} Q_N / \rho_S U_{0S} Q_S$ was 0.07, where $\rho_N = 995.90$ kg/m^3 and $\rho_S = 996.26$ kg/m^3 are the densities of the two streams calculated based on the incoming stream temperatures $T_N = 29$°C and $T_S = 28$°C and the difference in the suspended sediment concentrations. So, in case DF the denser fluid is situated in the faster (Solimões) tributary. The density contrast is $\Delta\rho = 0.36$ kg/m^3. The area-averaged mean streamwise velocity and the mean flow depth inside the first two km of the main confluence channel are $U = 2.267$ m/s and $D \approx 30$ m, respectively. These values are chosen as the velocity and length scale used to present the simulation results in nondimensional form. They are also the velocity and length scales that control the generation of lateral intrusions in cases with sufficiently strong density contrast between the two tributaries.

The corresponding Richardson number, $\mathrm{Ri} = g\,|\Delta\rho|/\rho_N (D/U^2)$ was 0.046 corresponding to a densimetric Froude number $\mathrm{Fr}_\rho = 1/\mathrm{Ri}^{0.5} = 4.66$. Previous field and experimental studies conducted at small and medium size confluences have shown that density contrast effects should be expected to be significant for $\mathrm{Fr}_\rho < O(1)$ (e.g., see Cheng & Constantinescu, 2018; Horna-Munoz et al., 2020; Q. Lewis et al., 2020; Ramon et al., 2013, 2014; Jiang et al., 2023; Constantinescu & Gualtieri, 2024) with near bed intrusions of denser fluid forming for $\mathrm{Fr}_\rho < 5$–10. Moreover, for confluences with a sufficiently large angle between the two tributaries and for relatively large density contrast ($\mathrm{Fr}_\rho < 1$–2), the fluid from the denser tributary plunges downwards as it starts interacting with the lighter fluid originating in the other stream. It then moves beneath the lighter fluid to reach the opposing bank. Meanwhile, the lighter fluid also tries to preserve its original direction as it moves near the free surface toward the opposing bank downstream of the confluence apex. The end effect is that the free surface regions of denser and lighter fluid change sides in the main confluence channel (Horna-Munoz et al., 2020).

Two additional simulations were performed with the same bathymetry, free surface elevation and discharges in the two incoming streams. In the case with no density difference (NDD), the density contrast effects were set to zero, meaning that the simulation was run with Ri = 0 but with the same temperatures in the incoming streams. In case DS, the densities of the two incoming streams were switched, meaning the denser fluid was situated in the slower (Negro) tributary. The Richardson number in case DS was the same as for case DF. So, if density contrast effects are strong enough to generate a near-bed intrusion of heavier fluid, the intrusion is expected to propagate in opposite directions in the DF and DS cases. Though generally the Negro river contains lighter fluid, case DS allows to better understand how density contrast affects the flow physics and to separate between intrusions of fluid driven by planform geometry and bathymetric features of the confluence channel and intrusions driven by density contrast.

Figure 1 also contains a dashed line that corresponds to the middle distance between the two banks measured at the free surface of a given cross section. The dashed line also defines the origin of the transverse coordinate, y', used in plots showing the solution in a cross section. The position of $y' = 0$ in a given cross section is the same in all test cases. The distance, x', between the confluence apex and a given cross section is measured along the $y' = 0$ line.

3. Numerical Model, Boundary Conditions and Code Validation

The simulations are performed using the delayed version of DES (Rodi et al., 2013; Spalart, 2009) which is a large-eddy-simulation (LES) based technique that is becoming popular for river engineering applications due to its capability to accurately simulate complex flows at high Reynolds numbers while being computationally less expensive than well-resolved LES and more accurate compared to LES with wall functions (Keylock et al., 2012). DES was shown to give more accurate predictions than unsteady Reynolds-Averaged Navier Stokes (RANS). DES is as a hybrid non-zonal method blending a RANS model near the solid surfaces with LES away from these surfaces. This is achieved by modifying the turbulence length scale in the base RANS model (Spalart-Allmaras model) such that the turbulence length scale becomes proportional with the local grid spacing away from the solid surfaces, as in classical LES.

The incompressible Navier-Stokes equations are expressed in generalized curvilinear coordinates on a non-staggered grid and then integrated using a fully implicit, fractional-step method. An advection-diffusion equation is solved for the transported scalars (e.g., nondimensional temperature/density). The Boussinesq approximation is used to account for the effects of the (non-uniform) density on the velocity field. The convective terms in the momentum equations are discretized using a blend between the fifth-order-accurate, upwind-biased scheme and the second-order central scheme. All the other terms in the momentum and pressure-Poisson equations are approximated using second-order central differences. The discrete momentum (predictor step), scalar transport equations and turbulence model equations (i.e., transport equation for the modified eddy viscosity, $\tilde{\nu}$, in the Spalart-Allmaras model) are integrated in pseudo-time using the alternate direction implicit approximate factorization scheme. Time integration is done using a double time-stepping algorithm. The time discretization is second-order accurate. The code is parallelized using multiple-passing interface. More details on the flow solver and DES model are given in Constantinescu et al. (2002, 2011) and Chang et al. (2007).

The boundary conditions are identical to those used in previous numerical studies of flow and mixing at natural confluences conducted using the same code (e.g., see Constantinescu et al., 2011, 2012; Horna-Munoz et al., 2020; Jiang et al., 2023). Given that the Froude number in the confluence channels was less than 0.2, a symmetry (free-slip) boundary condition was used at the top (free surface) boundary. The flow was assumed to be fully developed in the two incoming streams. Precursor eddy-resolving simulations were conducted in straight channels of constant cross section with periodic boundary conditions in the streamwise direction to generate the velocity fields corresponding to fully developed flow in these channels. The cross sections of these channels were identical to that of the two inlet sections of the tributary channels. These flow fields were then fed through the two inlet sections in the confluent flow simulations. The solid boundaries were treated as no-slip, rough surfaces. The turbulence length scale close to the solid boundaries was estimated using $d = d_{\min} + k_s$, where $d_{\min}$ is the distance to the closest solid surface and k_s is the equivalent roughness height. In the present simulations, $k_s = 3d_{50}$. The equation solved to calculate the modified viscosity on the solid surfaces was $\partial\tilde{\nu}/\partial n = \tilde{\nu}/d$, where n is the local normal direction to the surface. A convective boundary condition was used at the outlet boundary (Rodi et al., 2013). This type of boundary condition is commonly used in eddy resolving simulations as it allows the turbulent eddies to leave the computational domain in a physical way. Moreover, the generation of spurious oscillations near the outlet boundary is minimized (Constantinescu et al., 2011).

The nondimensional temperature/density in case DS and case DF and the nondimensional temperature in case NDD is defined as $\mathrm{TN} = (T_N - T)/(T_\mathrm{N} - T_\mathrm{S})$, where $T(x, y, z, t)$ is the dimensional temperature field. In case DF, TN = 1 corresponds to the heavier (colder) fluid in the Solimões tributary, while TN = 0 corresponds to the lighter fluid in the Negro tributary. The situation is reversed in case DS. This is why, 1-TN is generally plotted for case DS when comparing the nondimensional density/temperature fields with those in case NDD and case DF. The normal gradient of TN is set equal to zero at the solid boundaries, at the outlet boundary and at the top boundary. Once the governing equations are nondimensionalized using D and U, the Boussinesq term in the vertical momentum equation is $-Ri*TN$. The molecular Schmidt number in the advection-diffusion equation solved for TN is equal to six.

The Gridgen software was used for mesh generation. The bathymetry data was read into the mesh generator. The final mesh contained close to 0.7 million cells in the free surface plane. The mesh was refined near the channel bottom, the bank lines and the confluence apex to resolve the attached boundary layers and the MI. The horizontal grid spacing was close to 0.15D away from the solid boundaries. The maximum grid spacing in the vertical direction was 0.05D with about 30 grid points placed between the bed and the free surface, which should be sufficient to capture the presence of SOV cells. This level of mesh refinement was similar to the one used in other studies of flow and mixing at natural river confluences conducted using the same code (e.g., see Cheng & Constantinescu, 2018; Jiang et al., 2023). The flow became statistically steady after about $2{,}000D/U$. Statistics were collected over $1{,}500D/U$. The time step in the simulations was $\Delta t = 0.01D/U$ such that the Courant number was less than 0.1 for most computational cells during the simulation.

Directly relevant for the flows simulated in the present study, the DES solver was shown to accurately predict flow in strongly curved channels with natural bathymetry (Zeng et al., 2008) and the spatial development (e.g., streamwise variation of the width and shift of the mixing layer with the distance from its origin) and dynamics of coherent structures (e.g., size and frequency of passage of the vertical Kelvin-Helmholtz vortices)

10.1029/2025WR041934

in shallow mixing layers forming between parallel tributaries in constant-depth channels (Cheng & Constantinescu, 2020b). Validation of the solver for predicting mean flow, turbulence statistics and mixing at natural confluences with and without density contrast between the incoming streams is discussed by Constantinescu et al. (2011, 2012, 2016) and Horna-Munoz et al. (2020), who showed that DES accurately predicted the mean velocity, turbulent kinetic energy (TKE) and mean temperature distributions in relevant cross sections using the field data measurements of Sukhodolov and Rhoads (2001), Rhoads and Sukhodolov (2001) and Q. W. Lewis and Rhoads (2015).

4. General Features of the Free Surface Flow

The free surface distributions of the mean streamwise velocity and mean vertical vorticity are qualitatively similar in the three simulations. These distributions are shown in Figures 2a and 2b for case DF in which the faster stream (i.e., the Solimões tributary) contains the denser fluid. The bathymetry inside the Solimões tributary displays several interesting features. The deeper parts are situated over the right half of the cross section and a scour hole is present next to the right bank (RB) in the region where the bank curvature is the largest (Figure 1). This is why the highest streamwise velocities in between sections P2 and P6 are recorded near the RB. By contrast, very low streamwise velocities are predicted near the shallower regions close to the banks in the two tributary channels converging toward the confluence apex. The core of high velocities between sections P6 and P9 is not exactly situated over the deepest parts of the bathymetry. Rather the core remains on the right side of the main confluence channel. Meanwhile, downstream of section P5, the slow fluid originating in the Negro tributary accelerates fast and is squeezed in between the left bank (LB) and the core of high streamwise velocities. Another effect of the sudden change in the direction of the flow near the RB downstream of section P5 is the formation of two small regions of recirculating flow penetrating until close to section P7 (Figure 2a). Similarly, the sudden change in the orientation of the LB near section P8 induces a small recirculation eddy (Figure 2a). Downstream of section P9, the flow becomes shallower and the flow depth in the cross sections becomes more uniform away from the two banks. As a result, the width of the core of high streamwise velocities increases and its centerline moves gradually closer to the centerline of the main confluence channel.

Given the large differences in the momentum flux, discharge and mean velocity between the two tributaries, it is not surprising that a strong shear layer of high positive vertical vorticity forms on the right side of the confluence apex in the mean flow in all three cases (e.g., see Figure 2b for case DF). This shear layer separates upstream of the apex region (see corresponding recirculation region in Figure 2a) due to the shape of the tributary bank line as it approaches the confluence apex and to the presence of a very shallow region close to the bank line which induces a strong reduction of the streamwise velocity. Such a shear layer that separates early was also observed to form at the Poyang Lake/Yangtze River confluence (Jiang et al., 2023) inside the Poyang Lake tributary that has a similar bathymetry to that of the Solimões tributary (i.e., flow is very shallow near the bank line ending at the confluence apex and very deep on the other side). Meanwhile, there is no evidence of the formation of even a weak shear layer on the left side of the confluence apex in Figure 2b, as is generally observed at least at concordant confluences with fairly regular bathymetries in the two channel tributaries. In the latter case, the stagnation zone is bordered by the separated shear layers on the two sides of the confluence apex and their interactions may result in the shedding of counter-rotating vortices inside the MI (Constantinescu et al., 2011, 2012). By contrast, the formation of only one separated shear layer in the present simulations means that only co-rotating vortices can be generated inside the upstream part of the MI and no wake mode can develop. This is confirmed by the instantaneous flow vertical vorticity field in Figure 2c. More specifically, a large KH vortex is present just upstream of section P5 in Figure 2c.

Another important observation is that the rapid rotation of the core of high velocities from the right tributary due to strong RB curvature leads to strong curvature effects inside the main confluence channel. This is confirmed by the high curvature of the separated shear layer between sections P2 and P6 in Figure 2b. Interestingly, field observations demonstrated that, for both low- and relatively high-flow conditions, flow realignment between the two tributaries ended at about less than 3 km downstream of the junction (Gualtieri et al., 2018). This rapid change of flow direction in the Solimoes flow (60°–70° in less than 3 km) is associated with the strong curvature effects observed in the numerical study. A MI with curvature in the streamwise direction is subjected to a destabilizing effect if the lower speed stream is on the outside of the curve and to a stabilizing effect if the higher speed stream is on the outside of the curve. So, the cases analyzed in this study correspond to an unstable turbulent MI as the higher speed stream is situated close to the inner bank (RB), while the lower speed stream is situated on the

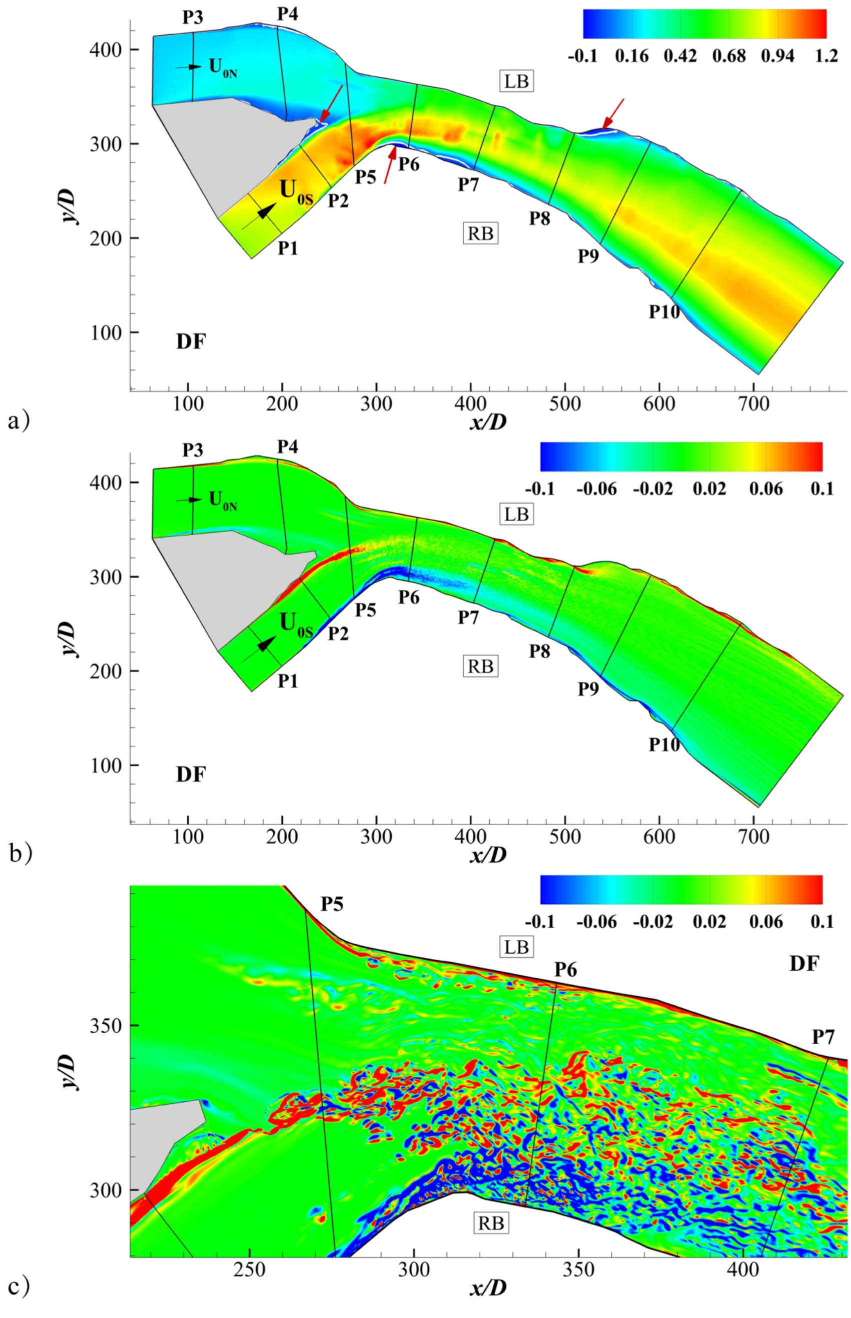

Figure 2. Flow structure at the free surface in case DF. (a) streamwise velocity, u/U, mean flow; (b) vertical vorticity, $\omega_z D/U$, mean flow; (c) vertical vorticity, $\omega_z D/U$, instantaneous flow. The white lines in frame a show the $u/U = 0$ contour. The red arrows point toward recirculation regions forming near the free surface.

"outer" bank side of the main channel. For such a case, the MI is subjected to destabilizing longitudinal curvature in the Taylor-Gortler sense (Plesniak et al., 1996), where curvature acts toward intensifying the rate of growth of the KH instabilities and vortices compared to a case where the MI is relatively straight. So, at least for case NDD, the vertical vortices generated inside the shear layer should be characterized by high rates of growth compared to cases where the same confluent flows will merge in such a way that the flow in the main channel is subject to negligible curvature effects.

The other shear layer present in Figure 2b forms at the RB downstream of section P5. This shear layer separates the core of high streamwise velocities from the right tributary from the region of slowly moving fluid near the RB.

In fact, the flow near the RB separates downstream of section P6 because of the high bank curvature in between sections P5 and P6, with a recirculation zone i.e. about 2.6 km long, for all the DES cases. Such inner-bank phenomena are similar to those observed in open channels of high curvature (e.g., see Constantinescu et al., 2013). A recirculation zone was also observed during both the field studies conducted in 2014 and 2015 at this confluence, being 1.0 km and more than 2.4 km long in low- and relatively high-flow conditions, respectively (Gualtieri et al., 2018; Trevethan et al., 2015). So, the predictions of DES for high flow conditions agree fairly well with the corresponding field observation. In the instantaneous flow (Figure 2c), the separation zone is characterized by the production of a wide range of energetic eddies. Besides the turbulent eddies associated with the MI and the shear layer and those generated by flow separation at the RB, additional turbulent eddies are generated by the interaction of the flow with the channel bed. More specifically, as the core of high velocities on the right side of the Solimões River moves over the deep region situated between sections P5 and P6, most of the near bed eddies generated by the interaction with the bed are entrained by the high-speed overflow and eventually raise to the free surface. This explains the presence of energetic eddies in between the MI and the shear layer forming next to the RB for $x/D > 300$ in Figure 2c. The flow also separates at the LB downstream of section P8, which induces the formation of another separated shear layer, also visible in Figure 2b, and the generation of smaller, but energetic, 3D eddies. However, these eddies do not interact with the MI. Their main role is to increase the local mixing.

5. Effect of Density Contrast on the Mean Flow and Turbulence Statistics

Despite the relatively small density difference, mainly induced by a temperature difference of only 1°C between the two streams, and the very large stream discharges (i.e., total confluence discharge close to 140,000 m^3/s), comparison of the nondimensional mean temperature/density fields in Figures 3a and 3b for case NDD (no density contrast, $Ri = 0$, $Fr_\rho = \infty$) and case DF ($Ri = 0.046$, $Fr_\rho = 4.66$), respectively, show that strong density contrast effects are present at the Negro/Solimões confluence. This finding is not surprising given that similar numerical and field investigations conducted for small and medium size confluences found that density contrast effects are significant for $Fr_\rho < 10$. For $2 < Fr_\rho < 10$, the main density contrast effect is the formation of a near bed intrusion of heavier fluid whose penetration length increases with the distance from the confluence apex. Field studies conducted at this confluence (Gualtieri et al., 2019) confirmed the presence of the near bed intrusion of heavier fluid entering the Negro River side of the post-confluence channel. However, at natural river confluences, a strongly tilted MI is not automatically related to the presence of density contrast as shown by the numerical investigation conducted by Jiang et al. (2023) at the Poyang Lake/Yangtze River confluence, i.e. a large aspect ratio (i.e., $W/D \approx 100$) confluence. The reason why these results are relevant for the present study is that the densimetric Froude number in the simulations corresponding to real conditions observed at that confluence ($Fr_\rho = 5.2$) is very close to the one of the present simulations despite the temperature difference being much larger ($\Delta T = 2.5$°C). Besides large differences in the size and flow discharge of the two confluences, the other main difference is that the secondary tributary is aligned with the downstream confluence channel at the Poyang Lake/Yangtze River confluence, while the opposite is true for the Negro/Solimões confluence.

Jiang et al. (2023) found that even if the water density in the incoming tributaries was equal, the boundaries of the MI became severely tilted, very similar to a case with density contrast. The same phenomenon is observed in case NDD (Figure 3a), where the MI tilts significantly downstream of section P5. Besides topographic steering effects driven by the main features of the irregular bathymetry, the main reason for the severe tilting is that the horizontal (streamwise) VR between the incoming streams is larger near the free surface compared to near the bed, where both velocities approach zero. So, near the free surface, the core of high velocities from the Solimões channel pushes more the MI toward the opposing LB compared to near the bed (see tilt of the MI boundaries in sections P7 and P9). The same phenomenon was also observed at the Poyang Lake/Yangtze River confluence where the tilting was in the opposite direction, as the major tributary was situated on the left side therein.

Before discussing the evolution of the MI in case DF, that corresponds to field conditions observed at the confluence in April/May 2015, one will first compare results for case NDD with those for case DS where the density contrast is such that it should act toward amplifying the tilting of the MI with respect to case NDD. Given that all other flow parameters are the same in the two simulations, differences between the mean nondimensional temperature/density fields in Figures 3a and 3c are entirely due to density contrast effects. Though qualitatively similar, the distributions of TN and 1-TN in the corresponding cross sections in Figures 3a and 3c, respectively, show large quantitative differences, as the density difference between the incoming flows increase the tilt of the

10.1029/2025WR041934

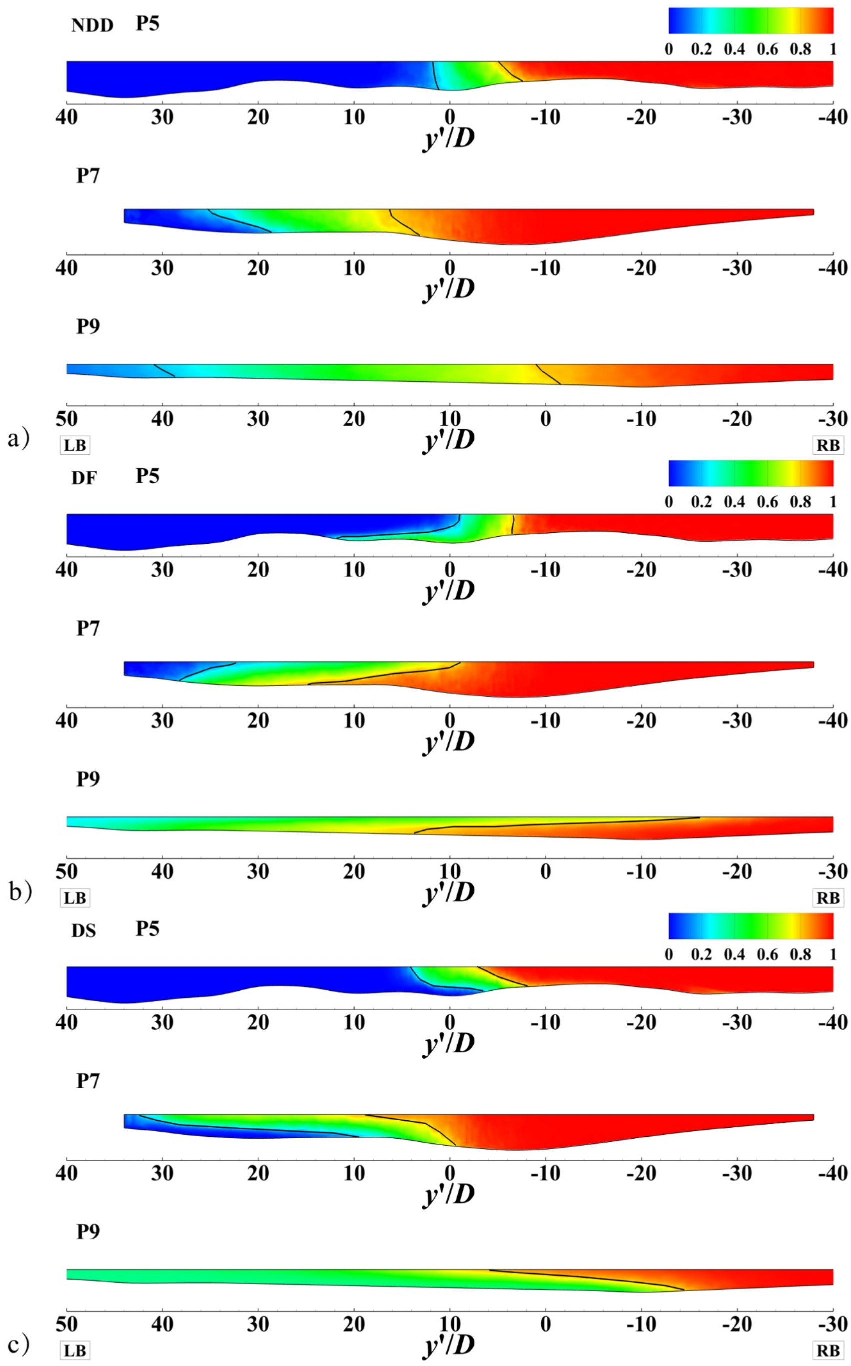

Figure 3. Nondimensional mean density/temperature in sections P5, P7, and P9. (a) TN, case NDD; (b) TN, case DF; (c) 1-TN, case DS. The black lines show the boundaries of the mixing interface (TN = 0.1 and 0.9) in the mean flow. The heavier fluid and the lighter fluid in the incoming streams are denoted HF and LF, respectively. The spanwise to vertical aspect ratio in the figures is 2:1.

MI boundaries in case DS. For example, in section P7, the lateral tilt of the MI boundary on the Negro side of the main channel increases from about 7D in case NDD to about 26D in case DS. This is due to the near-bed intrusion of heavier fluid from the Negro tributary moving beneath the mixed fluid inside the MI. The width of the MI boundary also increases on the Solimões side of the main channel, where an intrusion of lighter unmixed fluid forms near the free surface in case DS. By section P9, no unmixed fluid is left on the Negro side of the main channel in case DS, as the MI penetrates until the LB. On the Solimões side, the tilt of the MI boundary increases

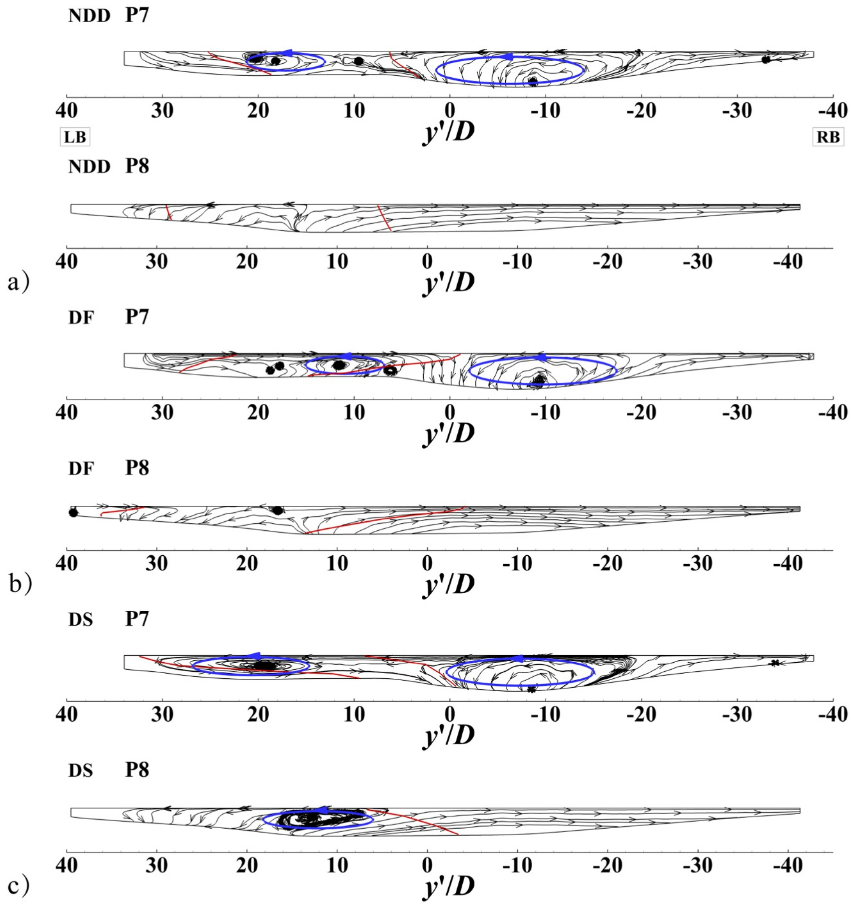

Figure 4. 2-D mean streamline patterns in sections P7 and P8. (a) Case NDD; (b) case DF; (c) case DS. The spanwise to vertical aspect ratio in the figures is 2:1. The red lines show the boundaries of the mixing interface (TN = 0.1 and 0.9) in the mean flow. Also shown are the main recirculation eddies and their sense of rotation.

from about 4D in case NDD to about 20D in case DS mainly due to the lateral growth of the free surface intrusion of lighter fluid.

Density contrast tries to tilt the MI in the opposite direction in case DF compared to case NDD. Results in Figure 3b show that stratification effects in case DF are strong enough to reverse the tilting of the MI observed in case NDD that was induced by the difference in the momentum and velocities between the two incoming streams and topographic steering. A near bed intrusion containing heavier fluid from inside the MI develops by section P5 in case DF. This intrusion penetrates beneath the lighter fluid originating in the Negro tributary. Meanwhile, there is no evidence of a lock-exchange-like flow developing near the MI boundary on the Solimões side of the post-confluence channel. This changes by section P7, where both MI boundaries are severely tilted, with a near bed intrusion of heavier fluid from the Solimões side of the main channel penetrating beneath the lighter mixed fluid inside the MI. By section P9, the MI penetrates until the LB. One should also mention that such a reversed tilting of the MI in the case with no density contrast compared to the case where density tries to tilt the MI in the opposite direction was also observed at the Poyang Lake/Yangtze River confluence. This suggests that a density contrast corresponding to a densimetric Froude number close to, or less than, five is sufficient for the tilt of the MI to be mainly controlled by density contrast effects.

Examination of the streamwise vorticity fields did not reveal the formation of SOV cells in any of the three simulations despite the large confluence angle. However, several cells of cross stream motion are present downstream of the confluence apex in the mean flow fields. These cells are visualized in Figure 4 at sections P7 and P8.

Though close to the confluence apex two small counter-rotating cells form in case NDD, two corotating cells are present starting at a small distance upstream of section P6 where curvature effects become important. The widths of the co-rotating cells forming on the left side and on the right side of the channel at section P7 are 9.1D and 25.7D, respectively. Though the cell closer to the LB is situated inside the MI at section P7, this cell forms initially on the Solimões side of the main channel before moving inside the MI as the flow moves past the high-curvature region present at the RB. The main mechanisms responsible for the generation of the two co-rotating cells are curvature effects associated with the region of high curvature near the RB and the rotation of the direction of the core of high velocities in the two tributaries downstream of the confluence apex. The sense of rotation of the two cells is consistent to that of the standard cell of secondary flow generated in a curved open channel in which the flow near the free surface moves from the "inner" bank, RB, toward the "outer" bank, LB, and in the opposite direction near the bed. The separated shear layer inside the Solimões tributary that penetrates way inside the main channel (Figure 2b) creates a sort of internal slip boundary that induces the formation of the two corotating cells, one of each side of the separated shear layer.

Cheng and Constantinescu (2022) have demonstrated that the development of the bottom and free surface intrusions of heavier and lighter fluid at confluences between parallel streams of unequal densities is accompanied by the generation of a strong cell of cross flow motion that advects free surface fluid toward the front of the lighter fluid intrusion and near-bed fluid toward the front of the heavier fluid intrusion, similar to the flow field generated in a temporally evolving lock-exchange flow. For the case of parallel streams, curvature effects are negligible. In the present cases with density contrast, both mechanisms (i.e., secondary cells associated with the spatially developing lock-exchange-like flow and curvature induced secondary flow) affect the generation and streamwise development of the cell that is situated inside the MI starting some distance from the confluence apex. Stratification effects are sufficiently strong in case DF (see section P7 in Figure 4b) such that the lock-exchange-like flow, rather than bank and flow curvature, determines the sense of rotation of the cell situated close to MI boundary with the region of unmixed fluid on the Solimões side of the main channel. This explains why this cell rotates in the opposite direction compared to the corresponding cell in case NDD (Figure 4a). By contrast, the cell forming outside the MI on the Solimões side of the main channel rotates in the same direction in Case NDD and in Case DF. Using the same arguments, the cell forming inside the MI in Case DS (Figure 4c) should rotate in the same direction as the corresponding cell in case NDD and its circulation is expected to be higher compared to case NDD, as both the lock-exchange flow and curvature effects try to rotate the fluid in the same direction. This is indeed what is observed when comparing the 2D streamline patterns in sections P7 and P8. The cell on the Solimões side of the post-confluence channel is still present at section P9 in case DS. By contrast, the corresponding cell in case NDD disappears around section P8 (Figure 4a). This shows that the overall coherence of the cell increases in case DS compared to case NDD. Moreover, this cell forms in a region containing mostly unmixed lighter fluid in case DS and rotates in the same direction as the corresponding cells forming in the other two cases. This is because the formation of this cell is mostly due to curvature induced effects.

The secondary-circulation cells forming at section P7 are the largest in case DS, where the widths of the cells forming on the left-hand side and on the right-hand side of the channel are 17.6D and 21.2D, respectively. The widths of the two cells in case DF are 10.8D and 16.4D, respectively. Interestingly, at the Yangtze River/Poyang Lake confluence dual counter-rotating helical cells and channel scale circulation with a width of 25 and 40 times the average depth therein, respectively, were observed as the Poyang Lake outflow channel acted as compound channel (high-flow conditions) and a single channel (low-flow conditions), respectively (Li, Tang, Yuan, Xiao, et al., 2022).

Comparison of the mean streamwise velocity in sections P6 to P9 in Figure 5 shows that the redistribution of the streamwise momentum in the CHZ is qualitatively similar in the three cases despite major differences in the position and tilting direction of the MI, and in the level of coherence and direction of rotation of the main cells of cross flow motion. One interesting feature is the formation of a secondary region of high streamwise momentum in between sections P6 and P8 adjacent to the main region of high-speed flow originating in the Solimões tributary. This region, present in cases with and without density contrast, is generated by the large-scale bed deformations downstream of section P6 and, in particular, by the increasing flow shallowness near section P7 (Figure 1a). The main quantitative effect due to density contrast is that the streamwise velocity becomes more uniformly distributed in the cross section as we move from a case with denser fluid in the faster Solimões tributary (case DF, Figure 5a), to a case with no density contrast (case NDD, Figure 5b) and, finally, to a case with reversed density contrast (case DS, Figure 5c). In particular, the peak values inside the core of high velocities on the

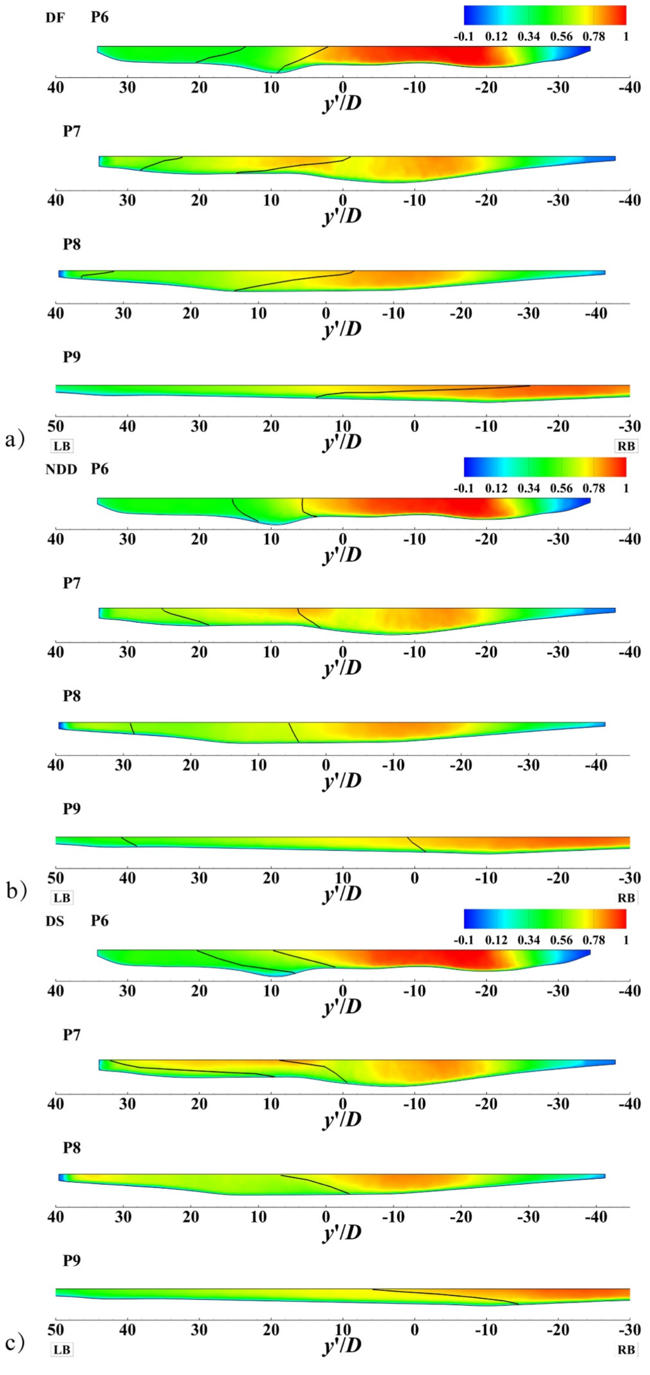

Figure 5. Distribution of mean streamwise velocity, u/U, in several cross sections. (a) Case DF; (b) case NDD; (c) case DS. The spanwise to vertical aspect ratio in the figures is 2:1. The black lines show the boundaries of the mixing interface interface (TN = 0.1 and 0.9) in the mean flow.

Solimões side of the post-confluence channel decay and the width of this region increases as we move from a case in which the faster tributary contains the heavier fluid to a case in which the faster tributary contains the lighter fluid.

Like the streamwise momentum, the free surface distributions of the nondimensional TKE in Figure 6 are qualitatively similar in the three cases. As expected, the TKE is amplified inside the separated shear layers forming near the LB of the Solimões River upstream of the junction and near the high curvature region at the RB. High TKE values are also observed in the region situated between the aforementioned shear layers where smaller-scale 3D eddies are generated starting midway between sections P5 and P6 (Figure 2c). The patches of high TKE present starting midway between sections P6 and P7 are mainly due to flow separation and generation of highly 3D energetic eddies as the flow moves over the deeper regions of the post-confluence channel (Figure 1a). The main quantitative effect is the monotonic decrease of the length and width of the region of high TKE induced by the passage of the KH vortices forming near the confluence apex as the difference between the density difference between Solimões and Negro tributaries changes from a positive value (case DF) to a negative value (case DS). The decay is relatively small if one compares case DF to case NDD, as also observed when comparing the TKE distributions in section P5 cutting through the separated shear layer forming close to the confluence apex (Figures 7a and 7b). These results suggest that the coherence of the KH vortices is comparable in the two simulations. The region of high TKE inside the separated shear layer becomes thinner and more tilted in case DS (Figure 7c), which suggests that once the water density becomes larger in the Negro tributary, the stretching of the cores of the KH vortices is stronger and dissipation increases. The KH vortices contain lighter (mixed) fluid in Case DS. As they advected along the boundary between the MI and the region containing unmixed heavier fluid, dissipation inside their cores increases sharply when they come into contact and try to entrain heavier fluid. This explains the faster decay of their coherence in case DS.

The mean flow distributions of the bed shear stress magnitude, τ_b, are qualitatively similar in the three cases. Figure 8 shows the predicted τ_b for case DF calculated using the law of the wall for rough surfaces together with the values inferred from the velocity measurements performed during the field study. In the latter case, the skin friction bed stress was calculated from the ADCP data using the quadratic-stress approach proposed by Sime et al. (2007) based on depth-averaged velocity and a zero-velocity height related to the bed grain size, namely d_{84}, which is bed grain diameter such that 84% of sediments are finer. The map of the skin friction bed shear stress was created by kriging the ADCP data.

There is good qualitative and even quantitative agreement between τ_b estimated based on the simulation and the field experiment (Figure 8). In both cases, the largest values correspond to the area of the main scour hole, which is 1,500 long, 700 m wide, and 70 m deep, and some distance downstream of it. So, bathymetry and the presence of regions of high flow depth appear to be the main factors influencing the bed shear stress distribution, with stratification playing a secondary effect. The lowest values of τ_b were predicted inside the Negro side of the confluence and beneath the stagnation and the separation regions on the Solimões side of the Amazon River. Peak values of around 8 Pa were predicted inside the Solimoes tributary and downstream of the confluence apex where the core of high velocity from the Solimoes tributary tries to maintain its direction and starts moving away from the RB. Though a core of high velocities also forms on the Negro River side of the

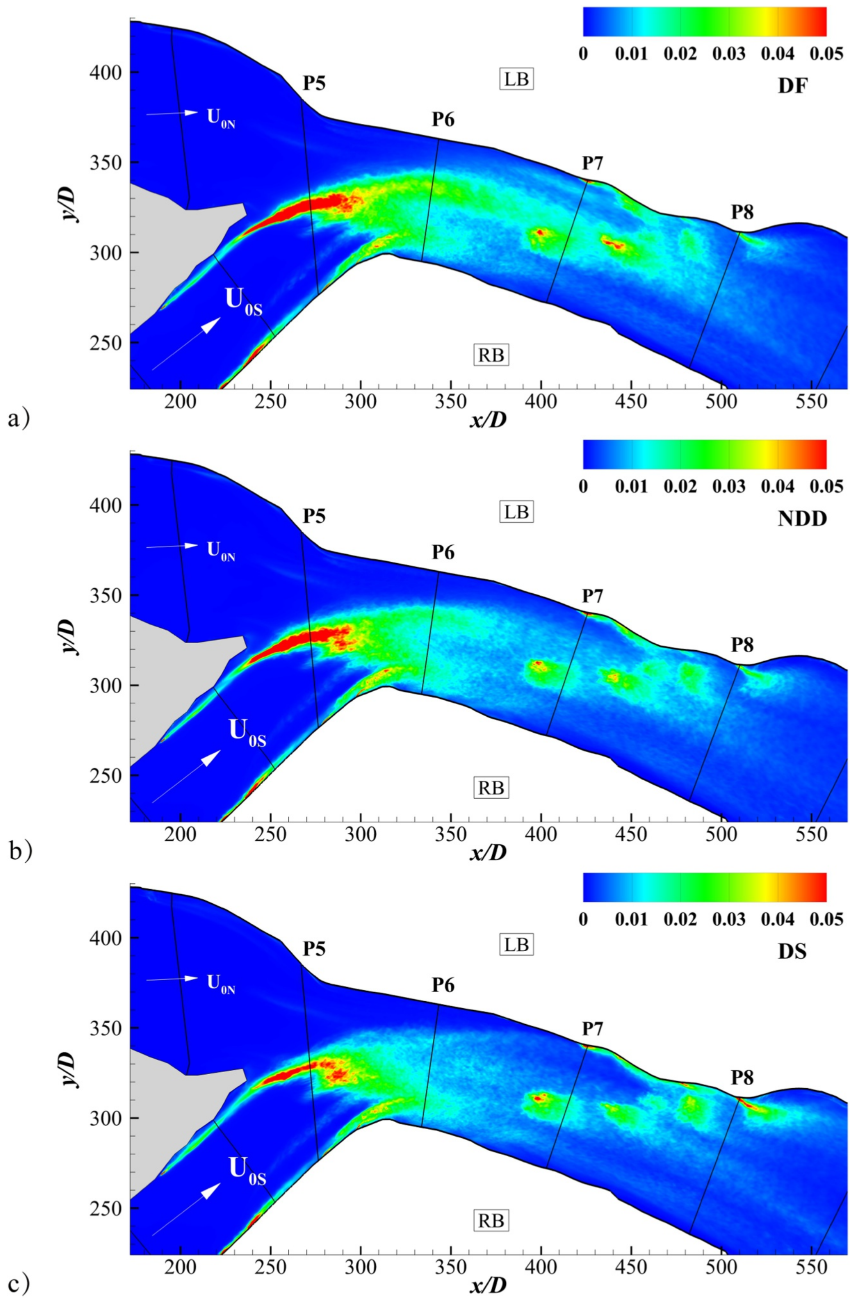

Figure 6. Turbulent kinetic energy, k/U^2, at the free surface. (a) Case DF; (b) case NDD; (c) case DS. The black lines show the boundaries of the mixing interface in the mean flow.

confluence, the region of high velocity magnitude never penetrates until close to the bed (e.g., see section P7 in Figure 5a), so its effects on the bed shear stress are relatively small.

6. Coherent Structures and Mixing Mechanisms

As already discussed in Section 4, KH vortices form over the downstream part of the separated shear layer forming on the Solimões River side of the confluence apex together with some small recirculation eddies in between the separated shear layer and the tip of the confluence apex. The effects of these vortices on the free surface mixing patterns in the instantaneous flow fields are visualized in Figure 9 for the case NDD with no density contrast. As expected, the recirculation regions contain mixed fluid, while the passage of the KH vortices

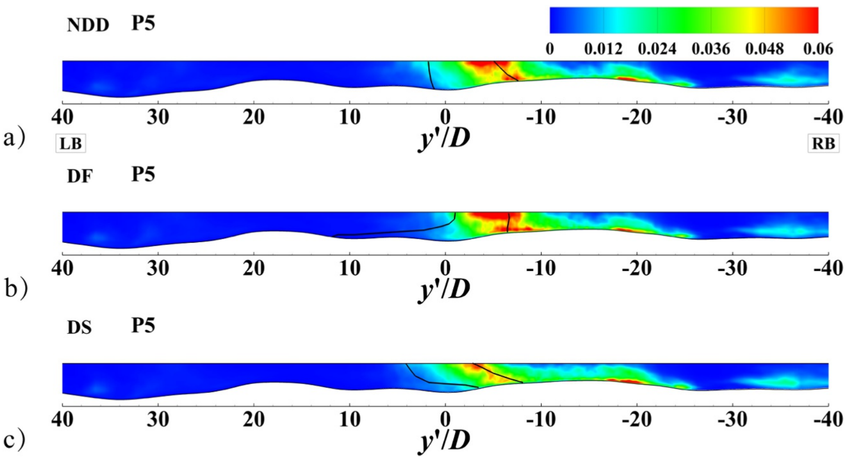

Figure 7. Turbulent kinetic energy, k/U^2, in section P5. (a) case NDD; (b) case DF; (c) case DS. The spanwise to vertical aspect ratio in the figures is 2:1. The black lines show the boundaries of the mixing interface (TN = 0.1 and 0.9) in the mean flow.

initially containing unmixed (red) fluid from the Solimões tributary induces mixing by engulfment of slower moving fluid from the Negro River as in a standard mixing layer forming between streams characterized by a large difference in their velocity. Examination of the instantaneous flow fields also shows that vortex pairing takes place inside the upstream part of the MI where the cores of these vortices are strongly coherent. Mixing is locally enhanced by such merging events that result in additional entrainment of fluid from the Negro River side of the main channel. The green arrows in Figures 8a and 8c point toward a larger vortex that just formed via vortex pairing. The mechanism is essentially the same as the one observed in mixing layers and shallow MI between non-parallel streams where the KH mode dominates (e.g., see Cheng & Constantinescu, 2021). This quasi-regular merging event taking place midway between sections P5 and P6 means that the dominant passage frequency, f, of the KH vortices reduces by a factor of 2. Indeed, the Strouhal number, $St = fD/U$ changes from about 0.02 at section P2 to about 0.01 at sections P6 and P7. However, not all KH vortices are subject to vortex pairing as they are advected in between sections P5 and P6, which is the main reason why smaller blobs containing mixed fluid are present in between larger blobs that formed via vortex pairing.

As the higher speed stream is situated near the inner (right) bank of the main channel, curvature induced effects are expected to increase the coherence and size of the KH vortices compared to a case where the planform geometry will not contain regions of strong bank curvature. Given that curvature at the RB increases suddenly midway between P5 and P6, and that curvature induced effects develop gradually, one expects these effects to peak some distance downstream of the region of high bank/channel curvature (Constantinescu et al., 2013), probably in between sections P6 and P7 and then do decay further downstream as the RB curvature reduces. The instantaneous temperature fields in Figure 9 show that the larger blobs forming via vortex pairing downstream of

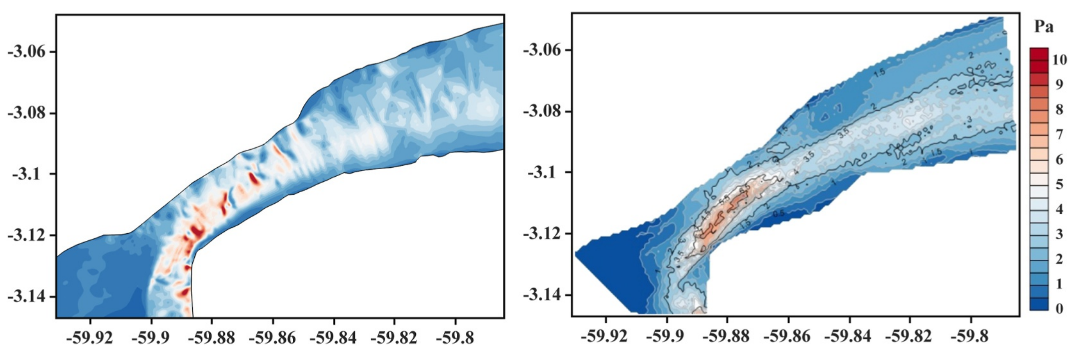

Figure 8. Mean bed shear stress, τ_b (Pa), for Case DF estimated based on the numerical simulation (left) and mean velocity field data (right).

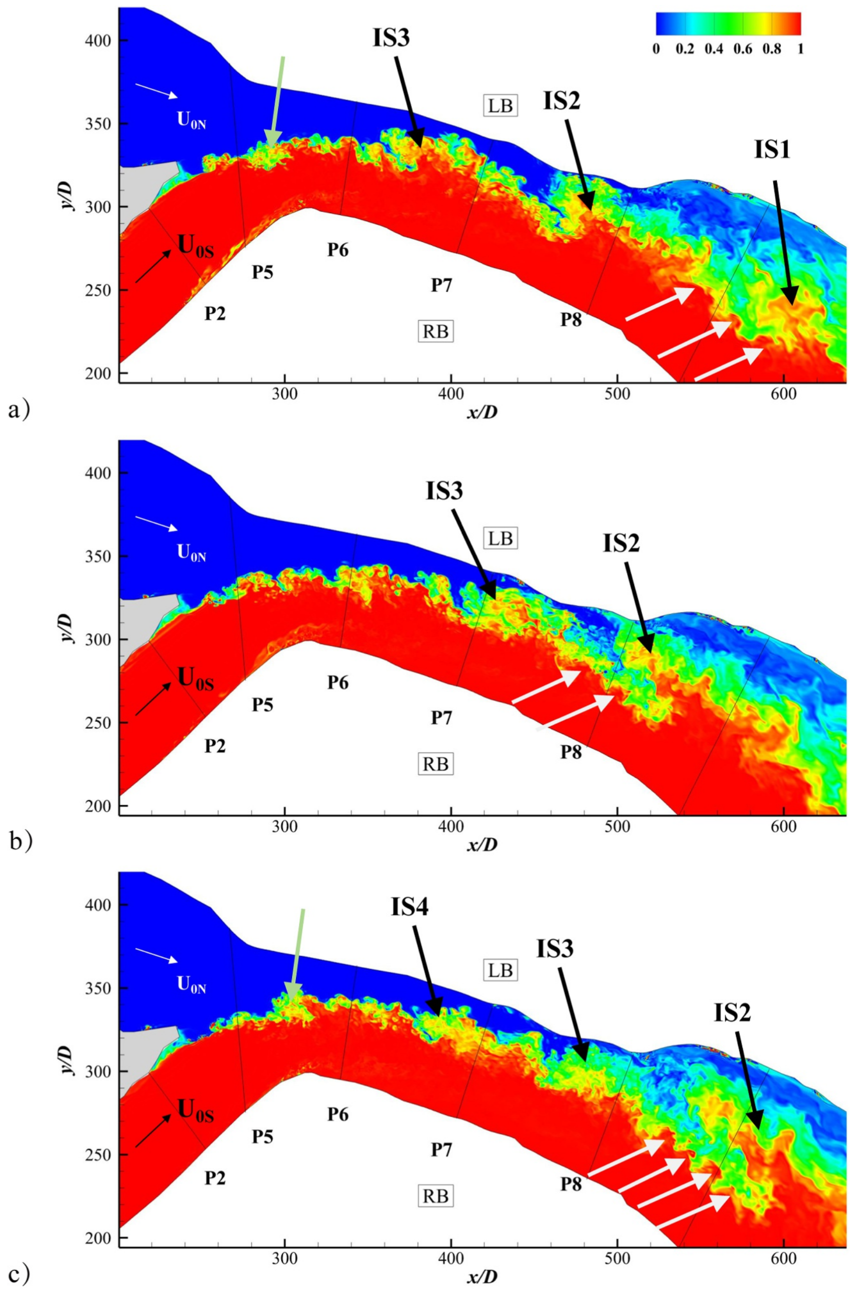

Figure 9. Free surface distribution of the nondimensional temperature, TN, in the instantaneous flow fields in case NDD. (a) $t = t_0$; (b) $t = t_0 + 80D/U$; (c) $t = t_0 + 160D/U$. Black arrows point toward large interfacial structures (IS) containing mixed fluid developing along the downstream part of the mixing interface (MI). The green arrow points toward a merging even occurring between two KH billows in between P5 and P6. Gray arrows point toward KH billows developing along the MI in between successive large IS.

section P5 undergo significant growth by the time they approach section P7, where they are labeled as interfacial structures (IS) (e.g., IS3 in Figure 8a and IS4 in Figure 9c). These IS containing mixed fluid are not undergoing merging as they are advected downstream of section P6. The size of the IS is growing as they are advected downstream. Their main growth mechanism is probably similar to that observed for shallow mixing layers between parallel and non-parallel streams in constant depth channels (Cheng & Constantinescu, 2020b, 2021) where once vortex pairing ceases, the circulation inside the KH vortices decreases and the cores of the KH vortices are severely stretched by the large mean shear across the MI before losing their coherence. The structure of the MI in

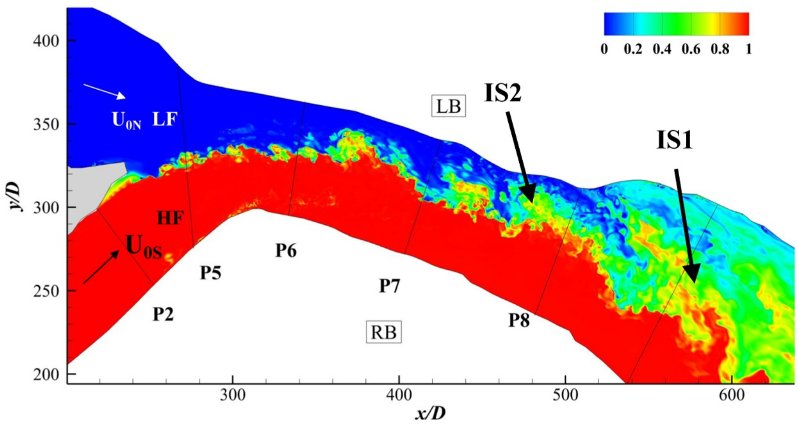

a)

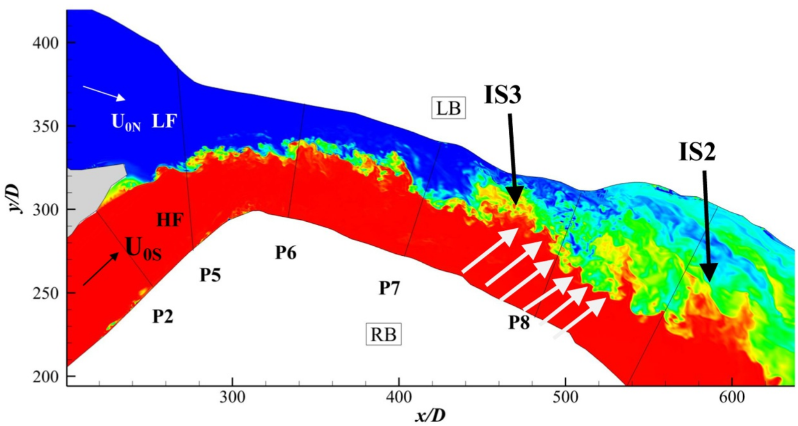

b)

Figure 10. Free surface distribution of the nondimensional density, TN, in the instantaneous flow fields in case DF. (a) $t = t_0$; (b) $t = t_0 + 140D/U$. Black arrows point toward large interfacial structures (IS) containing mixed fluid developing along the downstream part of the mixing interface (MI). Gray arrows point toward KH billows developing along the MI in between successive, large IS downstream of section P7. The heavier fluid and the lighter fluid in the incoming streams are denoted HF and LF, respectively.

the instantaneous temperature fields past section P7 in Figure 9 is similar to the one observed during the transition regime toward the quasi-equilibrium regime for MI forming in constant depth channels.

One interesting feature of the MI in Figure 9 is the formation of smaller-scale, mushroom-like intrusions of unmixed fluid from the faster tributary in between two successive IS. These eddies (see gray arrows in Figure 9) appear to be generated by smaller scale instabilities forming along the boundary between the mixed fluid inside the MI and the unmixed fluid from the Solimões tributary. The passage frequency of these eddies corresponds to a Strouhal number close to 0.04.

The presence of heavier fluid on the faster stream side of the main channel in case DF (Figure 10) does not induce any noticeable qualitative changes in terms of the vertical structures developing along the MI compared to case NDD (Figure 9). As the KH vortices contain heavier fluid, they maintain their coherence for a longer distance downstream of the confluence apex. On the other hand, their rate of growth is reduced by stratification effects. Large IS form downstream of section P7 (e.g., see IS1, IS2, and IS3 in Figure 10) and mushroom-like intrusions develop along the boundary between the MI region and the faster stream containing unmixed fluid. The average size of these intrusions is slightly smaller in case DF compared to case NDD, a similar effect to the one observed for the KH vortices present over the upstream part of the MI. The average Strouhal number associated with the passage of the interfacial coherent structures decays from 0.01 in case NDD to 0.0075 in case DF.

The fact that the sizes of the regions containing mixed fluid in a given cross section are larger in case DF compared to case NDD (e.g., see Figures 11a and 11b for section P6) is mostly due to mixing taking place beneath the free surface. As for the mixing observed in horizontal planes, coherent structures drive the mixing between the

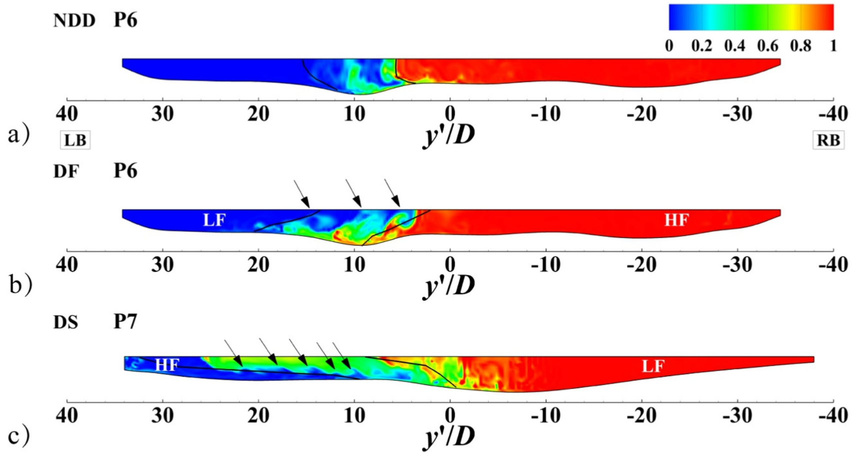

Figure 11. Nondimensional density/temperature in relevant sections in an instantaneous flow field. (a) TN, case NDD; (b) TN, case DF; (c) 1-TN, case DS. The black lines show the boundaries of the mixing interface (TN = 0.1 and 0.9) in the mean flow. The heavier fluid and the lighter fluid in the incoming streams are denoted HF and LF, respectively. The spanwise to vertical aspect ratio in the figures is 2:1.

intrusion of heavier mixed fluid and the unmixed lighter fluid from the Negro tributary (Figure 11b). Similar to a temporally evolving lock-exchange flow, where interfacial KH vortices form along the MI with the surrounding lighter ambient fluid and promote interfacial mixing, blobs of mixed fluid separate from the main body of the near bed intrusion in Figure 10b. This is the main mechanism by which stratification enhances mixing in case DF. As expected, this mechanism is absent in case NDD where the mixed fluid is mostly situated inside the cores of the KH vortices (Figure 11a).

Larger differences in the mixing patterns are observed in case DS (Figure 12). As already discussed, when analyzing the TKE distributions near the free surface, the fact that the KH vortices contain lighter fluid in case DS means they will dissipate and lose their coherence faster as they start interacting with the unmixed heavier fluid bordering the MI on the Negro River side of the post-confluence channel. This does not necessarily mean that free surface mixing will be reduced as once the cores of the KH vortices are stretched and break into smaller 3D eddies, these eddies are very efficient at locally enhancing mixing. However, as opposed to case NDD (Figure 9) and case DF (Figure 10), no evidence of formation of blobs of mixed fluid and associated IS is observed in the instantaneous density fields in Figure 12. The only coherent structures clearly visible in Figure 12 are some mushroom-like intrusions of lighter fluid from the Solimões River into the region containing heavier mixed fluid on the Negro River side of the main channel. These intrusions are clearly visible downstream of section P8. The Strouhal number associated with their passage frequency is about 0.03. Given that these intrusions form way downstream of the region of high curvature at the RB, it is unlikely their formation is due to curvature effects. The formation of mushroom-like eddies inside the downstream part of the MI is not surprising given that such eddies are usually generated via the Rayleigh-Taylor instability developing at the interface between two fluids of different densities, with the heavier fluid pushing the lighter fluid.

While important qualitative differences are observed between the vertical coherent structures playing a role in mixing in case DS and case DF, the coherent structures driving mixing associated with the development of the lateral intrusions of lighter and heavier fluid are qualitatively similar in these two cases. In case DS (Figure 11c) mixing is driven by the eddies developing along the boundary of the free surface intrusion of mixed fluid on the Negro River side of the main channel. By contrast similar eddies develop in case DF along the near bed intrusion of mixed fluid (Figure 11b).

Figure 13 compares the cross-sectional distribution of nondimensional density predicted by DES in an instantaneous flow field for case DF to the cross-sectional distribution of the short-time average acoustic backscatter intensity (BS) from the ADCP measurements carried out in the field in April/May 2015 at four key locations of the Negro/Solimões confluence. More specifically, sections C0, CNS5, CNS3, and A3 are located approximately 700, 1,600, 2,500, and 5,000 m downstream of the confluence apex, respectively. The ADCP data in Figure 12 were collected on 2 May 2015. In field studies the backscatter intensity is often applied, after proper calibration, as

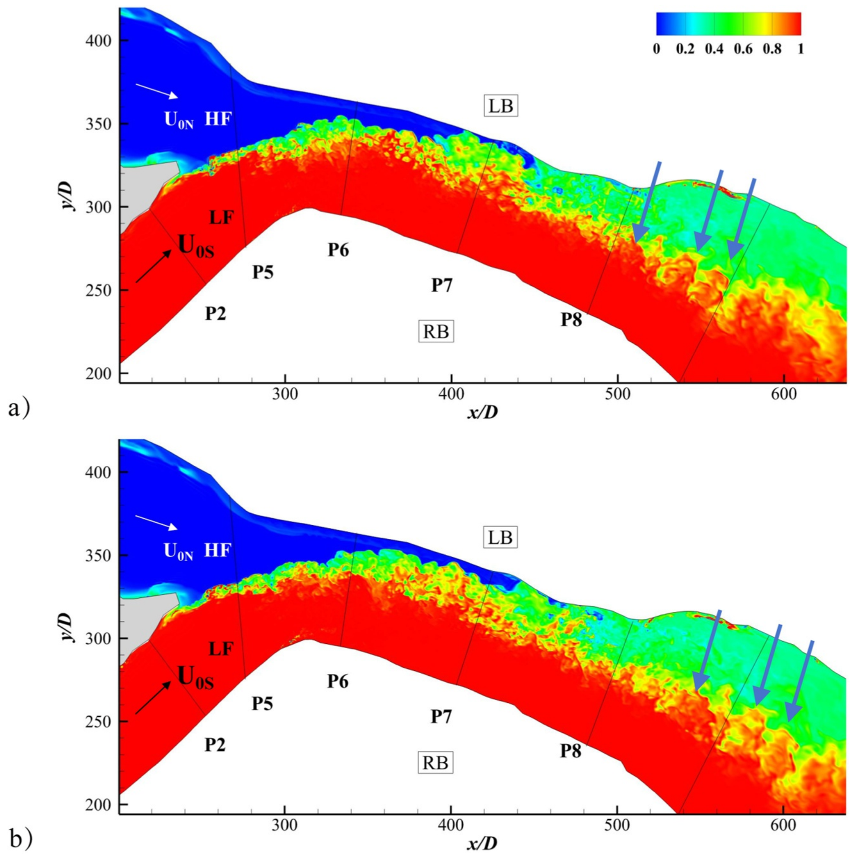

Figure 12. Free surface distribution of the nondimensional density, 1-TN, in the instantaneous flow fields in case DS. (a) $t = t_0$; (b) $t = t_0 + 160D/U$. Blue arrows point toward mushroom-like intrusions developing downstream of section P8 at the interface between the region containing unmixed fluid on the right side of the confluence and the region containing mixed fluid on the left side. The heavier fluid and the lighter fluid in the incoming streams are denoted HF and LF, respectively.

a proxy of TSS concentration (Szupiany et al., 2009). Hence, the cross-sectional distribution of the acoustic backscatter was used to identify the spatial development of the plume of sediment-laden flow moving near the bed from the Solimões side to the Negro side of the post-confluence channel and the location of the MI (Gualtieri et al., 2019). Downstream of A3 the identification of the borders of MI at the bed and at the free surface became uncertain based on the field data.

Backscatter thresholds of BS > 85 dB and BS < 75 dB were used for the unmixed Solimões and Negro waters, respectively. The corresponding values of the temperature of the unmixed water originating in the Negro and Solimões Rivers where TN = 0 and 1. During the field study the extents of the MI was clearly discernible from the pure waters of the Negro ("black") and Solimões ("white") rivers as a blended color of the two waters. So, formally the red and blue colors in the nondimensional density/temperature and backscatter intensity plots in Figure 12 correspond to unmixed water from the Negro and Solimões Rivers, respectively.

Figure 13 shows good qualitative agreement between the numerical results and the field data with large interfacial eddies, similar to the classical KH billows observed in temporally-evolving lock-exchange flows, playing a major role in mixing between the near-bed intrusion and the lighter fluid above it. Both simulation and field measurements show that a continuous layer of mixed fluid develops by section A3 between the regions containing fluid originating in the two tributaries.

7. Effect of Density Constrast on Mixing

The mean flow distributions of TN at the free surface and near the bed surface in Figure 14 together with those at selected cross sections in Figure 3 allow understanding how density contrast in the incoming streams affects

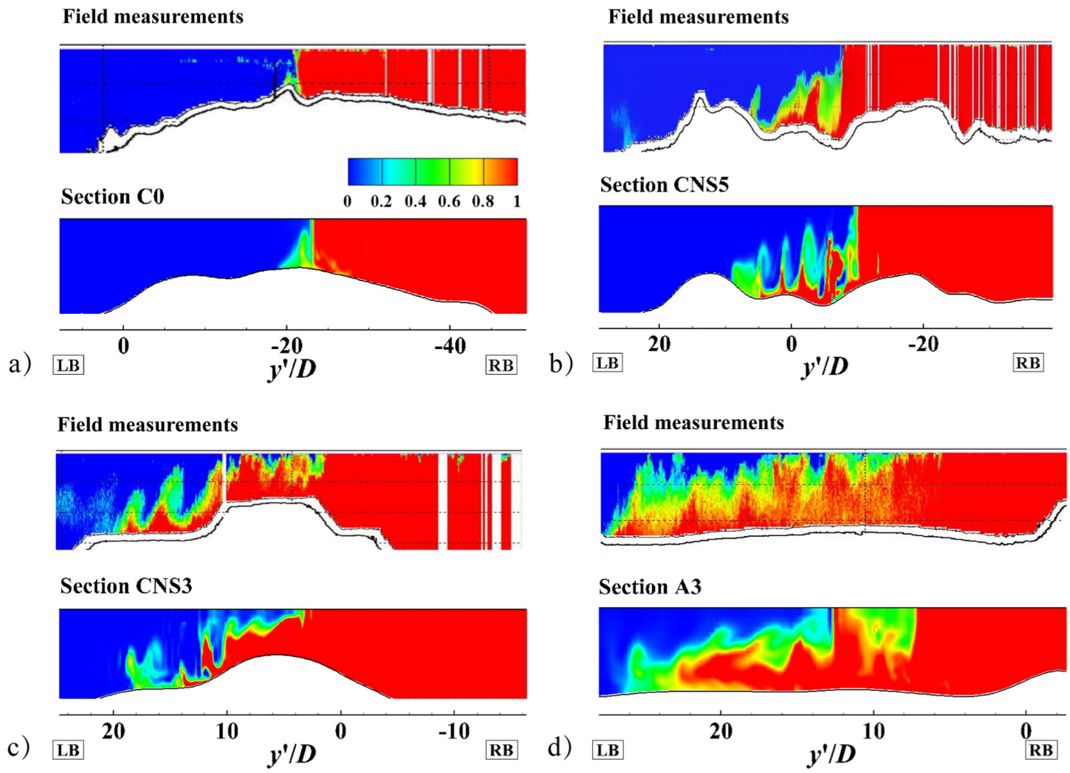

Figure 13. Visualization of the near bed intrusion of heavier fluid from the Solimoes river in several cross sections for Case DF. (a) section C0; (b) section CNS5; (c) section CNS3; (d) section A3. The bottom frames show the nondimensional temperature/density predicted by simulations in an instantaneous flow field. The top frames show the corresponding backscatter intensity data from field measurements obtained using short time averaging. The frames show only the region containing the near-bed intrusion in the cross section. The vertical to horizontal aspect ratio in the frames is larger than 1. The legend shown is for TN with TN = 0 corresponding to an average backscatter of 75 dB and TN = 1 corresponding to 85 dB.

mixing at the Negro/Solimões confluence. Consistent with the mixing patterns observed at other confluences for cases with negligible density contrast (e.g., see Horna-Munoz et al., 2020), the size and position of the region containing mixed fluid in case NDD (Figure 9a) are similar near the free surface and near the bed. In other words, the mixing is fairly uniform over the vertical direction if no density contrast is present. The main source of vertical nonuniformity of TN is due to topographic steering effects and the increase in the horizontal velocity difference on the two sides of the MI away from the bed that is, in particular, responsible for the tilting of the MI (Figure 3a). These effects are important in the region where the cores of high velocities from the two streams come into contact and in the region where the incoming streams realign with the centerline of the main channel (i.e., until section P8). No SOV cells are generated in case NDD. As a result, the width of the region of mixed fluid is not necessarily larger near the bed compared to near the free surface (e.g., see TN distribution in section P7 for case NDD in Figure 3a), as is generally observed at angled confluences where strongly coherent SOV cells form on one or both sides of the MI (e.g., see Constantinescu et al., 2011, 2012; Horna-Munoz et al., 2020).

The size and position of the region of mixed fluid are not anymore similar near the free surface and near the bed once sufficiently strong density contrast is present. For example, in case DF (Figure 14b) the left boundary of the MI close to the free surface is situated near the centerline of the main channel. Close to the bed, the same boundary migrates toward the LB. This is due to the spatially evolving lock-exchange-like flow (Figure 3b). As the heavier fluid reaches the left boundary of the MI, it starts plunging downwards. As it approaches the bed, this heavier fluid changes direction and pushes the left boundary of the MI toward the opposing bank line, LB. This phenomenon is responsible for the large degree of vertical nonuniformity of TN in the central part of the main channel downstream of section P5 in Figure 14b. Large differences in the mixing patterns are observed compared to the case with no density contrast. While some unmixed fluid is still present near the LB line until past section P10 in case NDD, the MI reaches the LB close to section P8 in case DF. The intrusion of mixed fluid close to the left boundary of the MI moves laterally on a (negatively) sloped bed surface toward the bank line. This induces lots of mixing

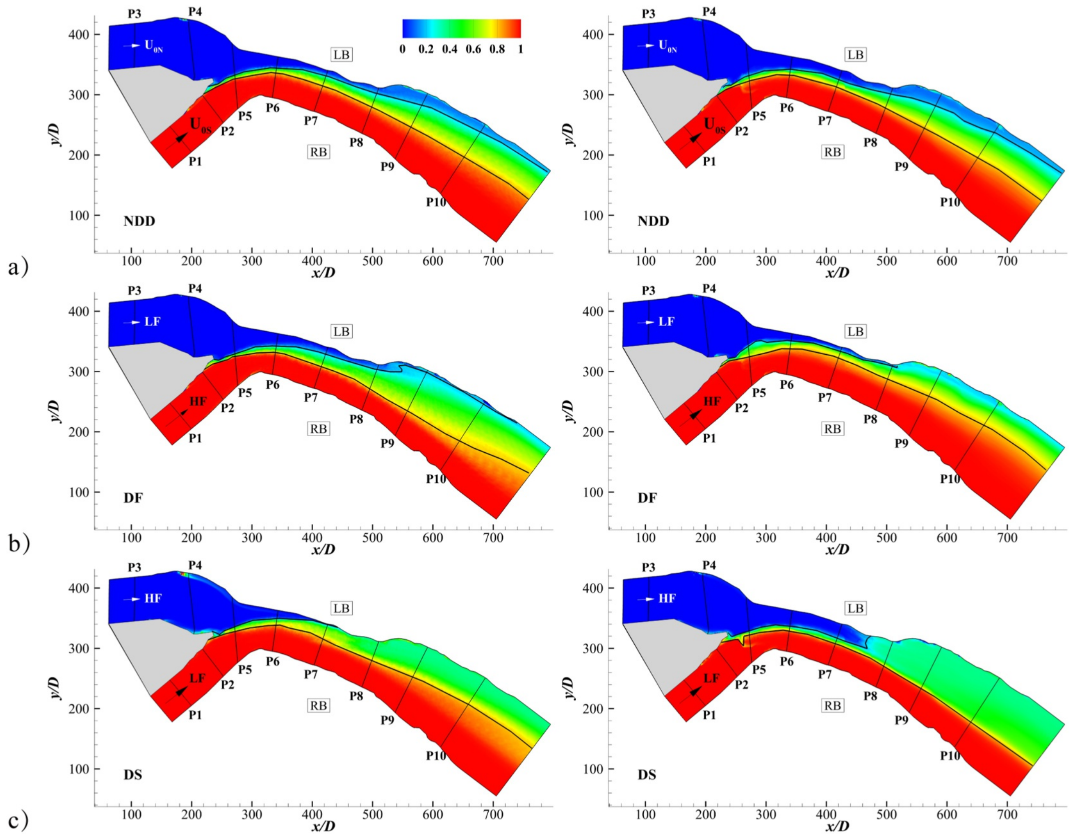

Figure 14. Nondimensional mean density/temperature at the free surface (left) and at 0.2D from the channel bottom (right). (a) TN, case NDD; (b) TN, case DF; (c) 1-TN, case DS. The black lines show the boundaries of the mixing interface (TN = 0.1 and 0.9) in the mean flow. The heavier fluid and the lighter fluid in the incoming streams are denoted HF and LF, respectively.

with the free surface, unmixed fluid originating in the Negro tributary. Similar to other confluences with moderate density contrast between the incoming streams for which $2 < Fr_\rho < 10$ (e.g., Horna-Munoz et al., 2020; Jiang et al., 2023), the vertical nonuniformity of the mean temperature field and the mixing between the fluids in the two tributaries in case DF are controlled by the development of the lock-exchange-like flow and associated secondary flow starting some distance from the confluence apex.

Qualitatively, the effect of density contrast between the incoming streams is the same in case DS (Figure 14c) and case DF (Figure 14b). As opposed to case NDD, the region of mixed fluid reaches the LB in the cases with density contrast. In fact, the MI reaches the LB earlier in case DS (i.e., around section P7 close to the free surface and midway between sections P7 and P8 near the bed) compared to case DF. The faster move of the MI toward the LB near the free surface in case DS (Figure 14c) is due to the near bed intrusion of lighter fluid originating in the Solimões River. The heavier fluid from the Negro River tributary is expected to push the MI toward the RB close to the bed. This is what happens between the confluence apex and about half distance between sections P7 and P8. The near-bed region of mixed fluid present next to the LB downstream of section P7 in Figure 14c is simply free surface mixed fluid that moves toward the LB and from there toward the bed due to the strongly coherent cell of secondary flow present in that region (Figure 4c).

Figure 15 compares the longitudinal development of the dimensionless width of the MI, $\delta(x')/W(x')$, predicted for case DF (filled circles) to that derived from the short-time average acoustic backscatter intensity (BS) measured in the field for the same case. The width of the MI at a given section is defined as the maximum spanwise distance between the fronts of the two intrusions near the bed and the free surface defined by the TN = 0.1 and 0.9 iso-contours. The numerical results match well with the field data until $x'/D = 150$. Larger differences are observed around $x'/D = 160$–170 where the field measurements predicted a decrease of δ/W due to the widening of the post-confluence channel.

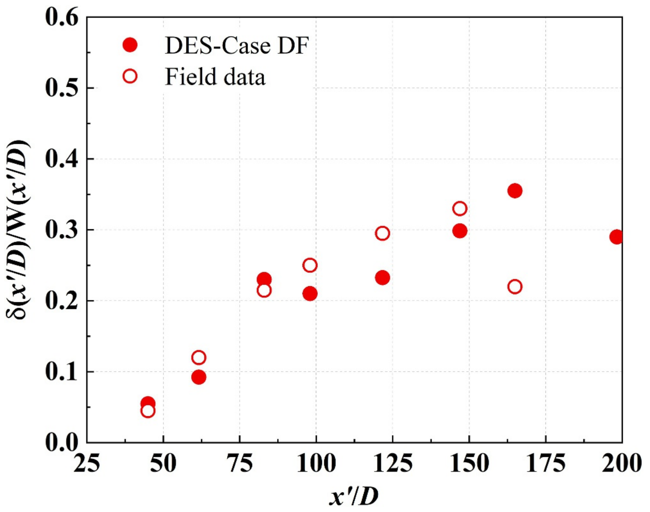

Figure 15. Nondimensional width of the mixing interface (MI), $\delta(x'/D)/W(x'/D)$, as a function of the streamwise distance from the confluence apex, x'/D, measured along the $y'/D = 0$ line (Figure 1). The width of the MI is calculated based on the boundaries of the MI near the bed and at the free surface shown in Figure 14.

The streamwise variation of the normalized volume of mixed fluid, $V_{mf}(x')/V(x')$, plotted in Figure 16 for the three cases describes in a more quantitative how fast the two streams mix once they come into contact near the confluence apex ($x'/D = 25$). The mixed fluid is defined as fluid with $0.1 < \text{TN} < 0.9$ and $V_{mf}(x')$ is the volume of mixed fluid in between the cross section passing through the confluence apex and the current cross section that is perpendicular to the centerline of the main channel. The total volume of fluid between the two cross sections is denoted $V(x')$, such that the ratio $V_{mf}(x')/V(x')$ is in fact the percentage of mixed fluid between the confluence apex and the current cross section. Figure 16 also includes the same ratio calculated using only a layer of thickness 0.2D starting at the free surface.

Consistent with available information obtained at both small and medium size concordant confluences with $2 < \text{Fr}_\rho < 10$ (e.g., Horna-Munoz et al., 2020; Jiang et al., 2023), the smallest overall mixing rate is observed in the case with no density contrast. Near $x/D = 450$, the percentage of mixed fluid is about 20% in case NDD, 23% in case DF and 27% in case DS. So, density contrast enhances mixing between the two streams, with most of the stratification driven mixing occurring beneath the free surface along the interface between the two lateral intrusions and the surrounding lighter/heavier unmixed fluid from the two tributaries.

Not surprisingly, given the free surface and near-bed mixing patterns in Figure 14a, the streamwise variation of $V_{mf}(x')/V(x')$ calculated based on the near mixing in case NDD is very similar to the one obtained based on mixing over the full depth. The errors in estimating mixing based on the free surface patterns are also relatively low, though not negligible, in case DF. The largest errors are observed in case DS for $x'/D > 300$ where the percentage of mixed fluid estimated based on the free surface patterns overestimates the actual percentage of mixed fluid inside the main channel. By $x'/D = 450$, the overestimation of V_{mf}/V is of the order of 25%–30% in case DS. This is important given that the standard way to estimate mixing rates at large size confluences is based on mixing patterns inferred from aerial pictures and videos.

8. Discussion

Besides its large size and large aspect ratio, the Negro/Solimões confluence is characterized by a complex planform geometry and complex bathymetry in the two tributaries and over the initial part of CHZ, upstream of the origin of the Amazon channel. The most important feature affecting flow hydrodynamics and mixing is the presence of a high curvature region at the bank bordering the high-speed stream which induces strong curvature effects that affect the development of the MI and triggers the formation of strong cells of cross flow motions inside the main confluence channel. The field studies conducted in 2014 and 2015 demonstrated that the common hydrodynamics features already observed in past confluence studies, such as stagnation zone, velocity deflection and re-alignment zone, maximum velocity region, separation region with recirculation, flow recovery region, are also present at the Negro/Solimões confluence (Gualtieri et al., 2018). However, while flow conditions do not appear to affect the extension of the velocity deflection and re-alignment zone, the recirculation and separation regions were longer (i.e., the separation zone increased from 2.5 to 4.0 km), the region of maximum velocity moved downstream, and the length of the CHZ was slightly larger for the relatively high-flow conditions considered in the present simulations (Gualtieri et al., 2018). Present results show no evidence of the formation of SOV cells, suggesting that one of their main geometrical drivers is a relatively small channel aspect ratio.

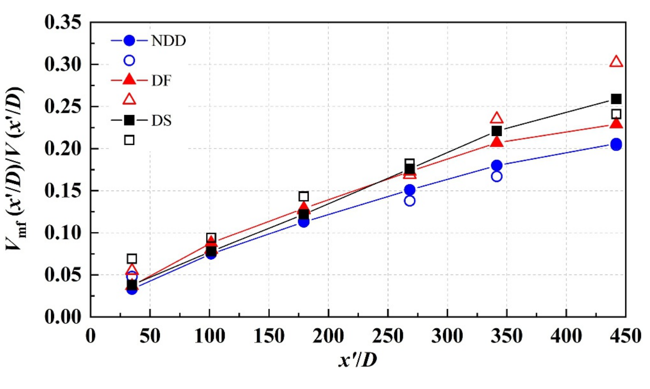

Figure 16. Nondimensional volume of mixed fluid, $V_{mf}(x'/D)/V(x'/D)$, as a function of the distance from the confluence apex measured along the mixing interface centerline, x'/D. The volume of the main channel between the confluence apex and the cross section at x' is $V(x'/D)$. The open symbols show the nondimensional volume of mixed fluid calculated based on the distributions of the nondimensional mean density/temperature near the free surface.

Density contrast effects appear to be primarily a function of the densimetric Froude number, Fr_ρ, regardless of the size of the confluence and channels aspect ratio. Despite the very large discharge and the relatively small temperature/density between the tributaries, the large water depth at the Negro/Solimões confluence resulted in a densimetric Froude number based on average velocity/depth in the post-confluence channel close to 5. Similar to other smaller-size confluences where the density contrast was such that $2 < Fr_\rho < 10$ (e.g., Horna-Munoz et al., 2020; Jiang et al., 2023), lateral intrusions of heavier, near-bed fluid and of lighter, free-surface fluid formed near the two boundaries of the MI, consistent with the development of a lock-exchange-like flow away from the confluence apex. Importantly, such large lateral intrusions and a strongly tilted MI were found to develop even without a density contrast (i.e., case NDD) because the streamwise VR between the tributaries is larger near the free surface than near the bed. Hence, the high velocity core from the faster Solimões channel pushes the MI toward the opposing LB more at the free surface than near the bed. In turn, the density contrast can act in favor/against of such shear-induced tilting resulting in increasing the tilting or even in reversing the tilting, if the density-driven tilting develops in the same or in the opposite direction as the shear-induced tilting.

Results obtained at the Negro/Solimões and the Poyang Lake/Yangtze River confluences suggest that for $Fr_\rho < 5$ the tilting direction of the MI is controlled by density contrast independently of the direction of tilting of the MI in the absence of density contrast. As for all numerical studies conducted at smaller natural river confluences with $Fr_\rho < 10$, the density contrast at the Negro/Solimões confluence was found to increase the speed of mixing between the confluent flows. These results are consistent with those of other studies conducted at large size and large size confluences. Lane et al. (2008) compared mixing processes at the large-scale ($W/D > 100$), discordant bed (≈15 m) confluence between Rio Paranà and Rio Paraguay at two occasions during February 2004 and May 2005, when complete mixing occurred at only 8 km from the confluence apex (rapid mixing) and at more than 400 km from it (slow mixing), respectively. The study revealed the different structure of the flow at the confluence at the two occasions and the role of bed discordance, momentum flux ratio and differences in water density. Turbulence-driven processes associated with the near-vertical MI (i.e., consistent with a small density contrast) resulted in slow mixing, while turbulence-driven processes associated with the near-horizontal MI, where Rio Paraguay flows under Rio Paranà, which has its bed above, resulted in channel-scale circulation and rapid mixing (i.e., consistent with a high-density contrast). Even the field studies conducted in 2014 and 2015 at the Negro/Solimões confluence highlighted an impact of flow conditions on mixing process as, for example, the width of the MI immediately downstream of the confluence apex was smaller in relatively high-flow conditions than in low-flow conditions (i.e., O(10 m) versus O(100 m)). This suggests a different intensity of mixing between the two field surveys driven by differences in Fr_ρ, which is consistent with what was observed at the Rio Paranà/Rio Paraguay and Poyang Lake/Yangtze River large-aspect ratio confluences (Lane et al., 2008; Xu et al., 2022) and in the present study.

At the Negro/Solimões confluence, curvature effects were responsible for the generation of two cells on the two sides of the MI, with one of these cells moving inside the MI at larger distances from the confluence apex. With no density contrast, the direction of flow rotation inside the two cells was consistent with the one expected in a curved channel in which the inner bank corresponded to the RB of the main confluence channel. In the case of a shallow mixing layer between parallel streams with $Fr_\rho < 10$, the development of a lock-exchange-flow is accompanied by the generation of a cells of cross flow motion in between the fronts of the two lateral intrusions (Cheng & Constantinescu, 2022). Its direction of rotation is determined by the direction of the flow near the bed and the free surface inside the lock-exchange flow. This flow is oriented toward the two fronts on the two sides of the lock-exchange flow. Thus, such a cell will rotate in opposite directions in case DF and case DS. Present results show that if $Fr_\rho < 5$ density contrast is sufficient to reverse the direction of rotation of the cell forming inside the MI in the absence of density contrast. Meanwhile, a strong increase in the coherence of this cell is observed in case DS with respect to case NDD. So, for the flow conditions considered in this study, stratification effects dominate curvature induced effects in terms of the main patterns of secondary flow.

Despite the large effects of density contrast on the secondary flow and mixing patterns at the Solimões/Negro confluence, the redistribution of the momentum inside the CHZ was mostly controlled by the planform geometry (i.e., confluence angle, bank curvature) and bathymetry. In fact, the field studies conducted in 2014 and 2015 suggested that momentum transfer between the tributaries was comparatively weaker in 2015, under high-flow conditions. Furthermore, the field observations highlighted the role of bedrock terraces about 20 m high, located approximately 2,200 and 2,500 m downstream of the confluence apex, just upstream of the entrance of the Amazon channel, to locally drive and modify the near-bed flow patterns of the denser waters moving from the Solimões side to the Negro of the CHZ (case DF). In addition, even at about 700 m downstream of the entrance of the Amazon channel (i.e., around section A14 in Figure 1), the structure of the density current was modified by the presence of a large step with a width of around 200 m and more than 30 m deep. The water depth was larger than

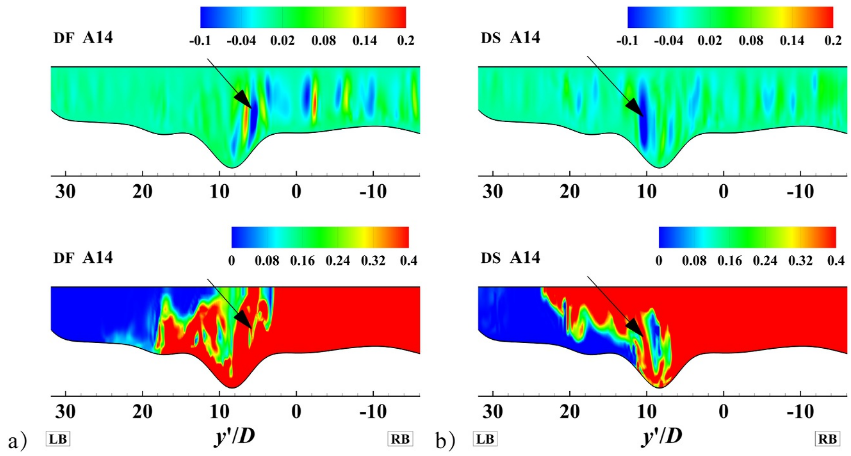

Figure 17. Patterns of nondimensional vertical velocity, w/U, (top) and nondimensional density, TN, (bottom) in section A14 around the location where the near-bed intrusion of heavier fluid is present. (a) Case DF; (b) Case DS. The vertical to horizontal aspect ratio in the frames is 10. The arrows point toward the main region of negative (toward the bed) velocity developing over the deepest part of the cross section.

75 m over the deepest parts of this bathymetric feature which likely represents the location of a past scour hole of the confluence (Ianniruberto et al., 2018). Comparison of the nondimensional distributions of the nondimensional vertical velocity in section A14 in Figure 17 show marked differences in the position and size of the main region of flow downwelling in the vicinity of the scour hole between cases DF and DS. The main region of flow downwelling is always situated on the downslope of the scour hole with respect to the "advancing" near-bed intrusion of heavier fluid, which explains its different position in cases DS and DF in Figure 17. Moreover, this downwelling cell also promotes engulfing and mixing as the cell advects lighter fluid from the free surface into the body of the intrusion (see arrows in Figure 17). For case DF, the effects of the past scour hole on the structure of the density current and the formation of a large cell of negative vertical velocities (Figure 17a) are consistent with field data measurements. Moreover, field data show that those local effects on mixing change from low-flow to high-flow conditions, which suggests the hydrological context plays an important role. It is also relevant to mention that using a timescale analysis Gualtieri et al. (2019) suggested bed friction and the change in channel width contribute to mixing but concluded that the differences in velocity and density between the tributaries were the dominant factors controlling confluence mixing.

The vortical structure of the MI far away from the confluence apex was markedly different from the one observed at other natural river confluences where the KH mode dominates. This was mostly due to the absence of any shear layer forming on the low-speed side of the confluence apex. Large vertical coherent structures in the form of large-scale IS developed at large distances from the confluence apex in the two cases where the density inside the core of the KH vortices was equal or higher than that in the slower tributary. Additional eddies were generated at the interface with the unmixed fluid from the Solimões side of the main channel in between successive, larger-scale IS. Such eddies did not form in the case where the core of the KH vortices contained lighter fluid. Additional coherent structures developed at one or both interfaces between the MI and the heavier/lighter fluid beneath/above it in the cases with density contrast. The action of these coherent structures was similar to that of the interfacial KH vortices forming in temporally evolving gravity current flows where these vortices eject heavier fluid from the body of the current into the surrounding ambient fluid. This is the main mechanism through which the intrusions of heavier and lighter fluid increase mixing between the two streams and ultimately explains why the overall rate of mixing between the two streams is larger in the simulations with $Fr_\rho \approx 5$ compared to case NDD. A comparison between the cross-sectional distribution of nondimensional density predicted by DES in an instantaneous flow field for case DF to the cross-sectional distribution of the short-time average acoustic backscatter intensity (BS) from the ADCP measurements at four key locations of the confluence revealed a reasonable agreement between the numerical results and the field data and confirmed the presence of KH-like structures along the interface between the heavier intrusion and the surrounding fluid. In addition, the simulation of case DF was able to match reasonably well the longitudinal development of the dimensionless width of the MI derived from the field measurements.

As in Case DF the near-bed intrusion of denser fluid from the Solimões River into the Negro River is associated with a sediment-laden flow in the field, the numerical results presented in this study offer relevant information to understand sediment dynamics and water chemistry patterns at this large confluence. Point-based and cross-sectional measurements obtained from the field using water sampling (ADCP), multibeam echo sounder, and multiparametric probe profiling provide only limited information on such dynamics, while remotely sensed studies based on the analysis of water surface reflectance yield an incomplete picture of mixing patterns (Kwon et al., 2023; Mohsen et al., 2021; Park & Latrubesse, 2015; Umar et al., 2018). The present numerical study clarified the spatial development of the sediment-laden flow from the Solimões River to the Negro River and its interaction with the post-confluence channel bathymetry, which is highly asymmetric. For example, in a single cross section, the depth can range from 10 m near the LB to approximately 60–70 m near the RB of the channel. Beyond the large difference in TSS (Table 1), the two tributaries have different water chemistry characteristics related to distinct hydro-ecological environments. The Negro River dark water tends to be highly acidic (pH ranged approximately 3.8–5.6) due to the high concentration of organic compounds and has a low conductivity (<15 μS/cm), while the pH of Andean white water is often near, or above, neutral, has a large conductivity (≈80 μS/cm) and absorbs less heat than the dark water (Gualtieri et al., 2018; Park & Latrubesse, 2015). The present numerical study provided a clear spatial identification on how the near-bed intrusion of denser fluid from the Solimões River is compressing the Negro waters to the LB to form a black water corridor with potential implication for fish ecology and biogeography, as several studies have demonstrated that some fish sub-species only exist in black or clear waters rivers in the Amazon Basin (Borges et al., 2023; Dagosta & de Pinna, 2019; Duncan & Fernandes, 2010). Hence, drastic changes in water chemistry occurring around confluences can act as a hydrographic barrier to some species and, as such, limit their migration.

9. Conclusions

A DES study was carried out to investigate the effects of density contrast between the tributaries on hydrodynamics, coherent structures and mixing at the confluence between the Negro and Solimões Rivers, Brazil, which was previously studied through field observations with ADCP, water sampling and multi-parametric probe. This confluence is characterized by both a large discharge (>100,000 m^3/s) and a large aspect-ratio (W/D > 100). Besides the DF case, which corresponds to the real relatively high-flow conditions in which Solimões River waters are denser than the Negro River waters, two additional cases, with no density contrast (NDD) and with reverse density contrast (DS), were considered keeping constant the other hydrodynamic parameters, which allowed separating density-contrast effects from those associated with planform geometry, bathymetry and, in particular, high curvature at the RB, something that is impossible to achieve using only data from field investigations where for a given set of flow conditions, the densities of the two streams are fixed. The main findings of this numerical study, the first reported in the literature for such a large river confluence using an eddy-resolving approach, can be summarized as follows:

1. The coherence and sense of rotation of the secondary-flow cells are a strong function of density contrast in the incoming streams. A densimetric Froude number lower than five is sufficient to reverse the sense of rotation of one of the main cells of secondary circulation with respect to the limiting case when the densities of the water in the two tributaries are equal, an effect associated with the development of a lock-exchange-like flow in transverse planes;
2. The presence of high curvature at the RB was the main reason the vortical structure of the MI was different from the one generally observed at angled confluences where the KH mode dominates. No shear layer was generated on the low-speed side of the confluence apex. This led to the formation of large-scale interfacial (vertical) structures and of additional smaller-scale instabilities especially in cases where the water density inside the core of the KH vortices was equal or higher than that in the slower (Negro) tributary;
3. The presence or absence of density contrast between the incoming streams affects the coherence of the vertical MI vortices and the large-scale mixing mechanisms inside and in the vicinity of the MI. These are the main factors that explain why the rates of mixing were higher in the cases with density contrast (DF and DS cases) compared to the case with no density contrast (NDD case);
4. No SOV cells form in the vicinity of the MI regardless of the presence, or not, of density contrast. Given that such a conclusion was also reached by Jiang et al. (2023) for a small discharge, high aspect ratio confluence, one can conclude that the confluence aspect ratio, W/D, is a main factor controlling the formation of SOV cells at confluences with a high confluence angle;

5. Simulations allowed to quantitatively characterize the effect of density contrast, or lack of it, on the variation of the volume of mixed fluid with the distance from the confluence apex and the errors associated with estimating mixing based on the free surface patterns at a complex bathymetry confluence. This is particularly important because the recent development of novel, cost-effective imaging techniques (i.e., thermal drone mapping) that can obtain the free-surface temperature map in a river over long distances using cameras installed on drones appears to be an appealing technique to characterize mixing at river confluences (Dugdale et al., 2019).
6. The complex planform geometry containing regions of very high RB curvature and several local bathymetric features, such as high bedrock terraces and deep past scour holes, largely affected flow structure and mixing patterns at the confluence between the Negro and Solimões Rivers.

Though the present study was limited to only one set of flow conditions, the present approach can be extended to cover additional relevant sets of flow, bathymetry and temperature/density differences. Of particular interest will be to study cases where the wake mode is expected to dominate inside the MI at this confluence. Understanding the complex interactions among density differences, curvature effects and local bathymetric features at such large-scale confluences is a prerequisite toward being able to use numerical approaches based on 3-D eddy-resolving simulations to understand transport mechanisms and make quantitative predictions related to the distributions of sediment concentration, food, variables characterizing water chemistry and, potentially, even fish biogeography patterns. This will require solving additional transport equations and possibly the use of Lagrangian approaches to track passive particles and/or fish.

Conflict of Interest

The authors declare no conflicts of interest relevant to this study.

Availability Statement

The data can be accessed online at https://doi.org/10.57760/sciencedb.34028.

Acknowledgments
The field data used in this study were collected within the Clim-Amazon Research Project funded by grant agreement FP7 INCO-LAB n°295091 from the European Commission. Carlo Gualtieri acknowledges the contribution to this Project from the colleagues Marco Ianniruberto, Naziano Filizola and Mark Trevethan. The numerical calculations reported in this paper were performed at TUBITAK ULAKBIM, High Performance and Grid Computing Center (TRUBA resources) and on the Argon High Performance Computer at the University of Iowa.

References

Arbat-Bofill, M., Palau, A., Sanchez-Junni, M., Castellet, E. B., Ninerola, D., & Dolz, J. (2014). Hydrodynamics of Ribarroja Reservoir (Ebro River, Spain): Water temperature, water velocities and water age. In A. Schleiss (Ed.), *Proceedings of the RiverFlow 2014 international conference on fluvial hydraulics, Lausanne, Switzerland*. Taylor and Francis.

Ashmore, P. E., Ferguson, R. I., Prestegaard, K. L., Ashworth, P. J., & Paola, C. (1992). Secondary flow in anabranch confluences of a braided, gravel-bed stream. *Earth Surface Processes and Landforms*, *17*(3), 299–311. https://doi.org/10.1002/esp.3290170308

Borges, S. H., D'Aquino, D. D., Victória da Cruz, M., & Felipe de Souza, R. (2023). Turnover in fish species composition is related to water color of Amazonian rivers. *Journal of Tropical Ecology*, *39*, e7. https://doi.org/10.1017/s0266467422000451

Bouchez, J., Lajeunesse, E., Gaillardet, J., France Lanord, C., Dutra Maia, P., & Maurice, L. (2010). Turbulent mixing in the Amazon River: The isotopic memory of confluences. *Earth and Planetary Science Letters*, *290*(1–2), 37–43. https://doi.org/10.1016/j.epsl.2009.11.054

Chang, K. S., Constantinescu, G., & Park, S. O. (2007). Assessment of predictive capabilities of detached eddy simulation to simulate flow and mass transport past open cavities. *ASME Journal of Fluids Engineering*, *129*(11), 1372–1383. https://doi.org/10.1115/1.2786529

Cheng, Z., & Constantinescu, G. (2018). Stratification effects on flow hydrodynamics and mixing at a confluence with a highly discordant bed and a relatively low velocity ratio. *Water Resources Research*, *54*(7), 4537–4562. https://doi.org/10.1029/2017WR022292

Cheng, Z., & Constantinescu, G. (2020a). Stratification effects on hydrodynamics and mixing at a river confluence with discordant bed. *Environmental Fluid Mechanics*, *20*(4), 843–872. https://doi.org/10.1007/s10652-019-09725-6

Cheng, Z., & Constantinescu, G. (2020b). Near-field and far-field structure of shallow mixing layers. *Journal of Fluid Mechanics*, *904*, A21. https://doi.org/10.1017/jfm.2020.638

Cheng, Z., & Constantinescu, G. (2021). Shallow mixing layers between non-parallel streams in a flat-bed, wide channel. *Journal of Fluid Mechanics*, *916*, A41. https://doi.org/10.1017/jfm.2021.254

Cheng, Z., & Constantinescu, G. (2022). Shallow mixing interfaces between parallell streams of unequal densities. *Journal of Fluid Mechanics*, *945*, A2. https://doi.org/10.1017/jfm.2022.505

Constantinescu, G. (2014). LE of shallow mixing interfaces: A review. *Environmental Fluid Mechanics*, *14*(5), 971–996. https://doi.org/10.1007/s10652-013-9303-6

Constantinescu, G., & Gualtieri, G. (2024). River confluences: A review of recent field and numerical studies. *Environmental Fluid Mechanics*, *24*(6), 1143–1191. https://doi.org/10.1007/s10652-024-10002-4

Constantinescu, G., Kashyap, S., Tokyay, T., Rennie, C. D., & Townsend, R. D. (2013). Hydrodynamics processes and sediment erosion mechanisms in an open channel bend of strong curvature with deformed bathymetry. *Journal of Geophysical Research: Earth Surface*, *118*(2), 480–496. https://doi.org/10.1002/jgrf.20042

Constantinescu, G., Miyawaki, S., Rhoads, B., & Sukhodolov, A. (2012). Numerical analysis of the effect of momentum ratio on the dynamics and sediment entrainment capacity of coherent flow structures at a stream confluence. *Journal of Geophysical Research*, *117*(F4), F04028. https://doi.org/10.1029/2012JF002452

Constantinescu, G., Miyawaki, S., Rhoads, B., & Sukhodolov, A. (2014). Numerical evaluation of the effects of planform geometry and inflow conditions on flow, turbulence structure, and bed shear velocity at a stream confluence with a concordant bed. *Journal of Geophysical Research: Earth Surface*, *119*(10), 2079–2097. https://doi.org/10.1002/2014JF003244

Constantinescu, G., Miyawaki, S., Rhoads, B., & Sukhodolov, A. (2016). Influence of planform geometry and momentum ratio on thermal mixing at a stream confluence with a concordant bed. *Environmental Fluid Mechanics*, *16*(4), 845–873. https://doi.org/10.1007/s10652-016-9457-0

Constantinescu, G., Miyawaki, S., Rhoads, B., Sukhodolov, A., & Kirkil, G. (2011). Structure of turbulent flow at a river confluence with a momentum and velocity ratios close to 1: Insight from an eddy-resolving numerical simulation. *Water Resources Research*, *47*, W05507. https://doi.org/10.1029/2010WR010018

Constantinescu, G., Pasinato, H., Wang, Y. Q., Forsythe, J. R., & Squires, K. D. (2002). Numerical investigations of flow past a prolate spheroid. *J. of Fluids Engineering ASME*, *124*(4), 904–910. https://doi.org/10.1115/1.1517571

Dagosta, F., & de Pinna, M. (2019). The fishes of the Amazon: Distribution and biogeographical patterns, with a comprehensive list of species. *Bulletin of the American Museum of Natural History*, *431*, 1–163. https://doi.org/10.1206/0003-0090.431.1.1

Dugdale, S. J., Kelleher, C. A., Malcolm, I., Caldwell, S., & Hannah, D. M. (2019). Assessing the potential of drone-based thermal infrared imagery for quantifying river temperature heterogeneity. *Hydrological Processes*, *33*(7), 1152–1163. https://doi.org/10.1002/hyp.13395

Duncan, W., & Fernandes, M. (2010). Physicocheimical characterisation of white, black and clearwater rivers of the Amazon River and its implications on the distribution of freshwater stingrays (Chondrichthyes, Potamotrygonidae). *Pan-American Journal of Aquatic Sciences*, *5*(3), 454–464.

Filizola, N., Spinola, N., Arruda, W., Seyler, F., Calmant, S., & Silva, J. (2009). The Rio Negro and Rio Solimões confluence point—Hidrometric observations during the 2006–2007. In *Cycle river coastal and estuarine morphodynamics: RCEM. 6th symposium on river, coastal and estuarine morphodynamics (RCEM 2009), Santa Fe (Argentina), September 21/25, 2009*.

Ford, D. E., & Johnson, M. C. (1983). An assessment of reservoir density currents and inflow processes. In *Technical Report E-83-7, U.S. Army Corps of Engineers Waterways Experiment Station, Vicksburg, Mississippi, USA*.

Gaudet, J. M., & Roy, A. G. (1995). Effect of bed morphology on flow mixing length at river confluences. *Nature*, *373*(6510), 138–139. https://doi.org/10.1038/373138a0

Gualtieri, C., Filizola, N., de Oliveira, M., Martinelli Santos, A., & Ianniruberto, M. (2018). A field study of the confluence between Negro and Solimões Rivers. Part 1: Hydrodynamics and sediment transport. *Comptes Rendus Geoscience*, *380*(1–2), 31–42. https://doi.org/10.1016/j.crte.2017.09.015

Gualtieri, C., Ianniruberto, M., & Filizola, N. (2019). On the mixing of rivers with a difference in density: The case of the Negro/Solimões confluence, Brazil. *Journal of Hydrology*, *578*, 124029. https://doi.org/10.1016/j.jhydrol.2019.124029

Gualtieri, C., Ianniruberto, M., Filizola, N., Santos, R., & Endreny, T. (2017). Hydraulic complexity at a large river confluence in the Amazon basin. *Ecohydrology*, *10*(7), e1863. https://doi.org/10.1002/eco.1863

Gualtieri, C., Martone, I., Filizola, N., & Ianniruberto, M. (2020). Bedform morphology in the area of the confluence of the negro and Solimoes-Amazon Rivers. *Brazil Water*, *12*(6), 1630. https://doi.org/10.3390/w12061630

Guillén-Ludeña, S., Cheng, Z., Constantinescu, G., & Franca, M. J. (2017). Hydrodynamics of mountain river confluences and its relationship to sediment transport. *Journal of Geophysical Research: Earth Surface*, *122*(4), 901–924. https://doi.org/10.1002/2016jf004122

Horna-Munoz, D., Constantinescu, G., Rhoads, B., Quinn, L., & Sukhodolov, A. (2020). Density effects at a concordant bed, natural river confluence. *Water Resources Research*, *56*(4), e2019WR026217. https://doi.org/10.1029/2019WR026217

Ianniruberto, M., Trevethan, M., Pinheiro, A., Andrade, J. F., Dantas, E., Filizola, N., & Gualtieri, C. (2018). A field study of the confluence between Negro and Solimões Rivers. Part 2: Bed morphology and stratigraphy. *Comptes Rendus Geoscience*, *350*(1–2), 43–54. https://doi.org/10.1016/j.crte.2017.10.005

Jiang, C., Constantinescu, G., Yuan, S., & Tang, H. (2023). Flow hydrodynamics, density contrast effects and mixing at the confluence between the Yangtze River and the Poyang Lake channel. *Environmental Fluid Mechanics*, *23*(2), 229–257. https://doi.org/10.1007/s10652-022-09848-3

Kenworthy, S. T., & Rhoads, B. L. (1995). Hydrologic control of spatial patterns of suspended sediment concentration at a small stream confluence. *Journal of Hydrology*, *168*(1–4), 251–263. https://doi.org/10.1016/0022-1694(94)02644-q

Keylock, C. J., Constant, G., & Hardy, R. J. (2012). The application of computational fluid dynamics to natural river channels: Eddy resolving versus mean flow approaches. *Geomorphology*, *179*, 1–20. https://doi.org/10.1016/j.geomorph.2012.09.006

Kwon, S., Won Seo, I., & Lyu, S. (2023). Investigating mixing patterns of suspended sediment in a river confluence using high-resolution hyperspectral imagery. *Journal of Hydrology*, *620*, 129505. https://doi.org/10.1016/j.jhydrol.2023.129505

Lambs, L. (2004). Interactions between groundwater and surface water at river banks and the confluence of rivers. *Journal of Hydrology*, *288*(3–4), 312–326. https://doi.org/10.1016/j.jhydrol.2003.10.013

Lane, S. N., Parsons, D. R., Best, J. L., Orfeo, O., Kostaschuk, R. A., & Hardy, R. J. (2008). Causes of rapid mixing at a junction of two large rivers: Rio Parana and Rio Paraguay. Argentina. *Journal of Geophysical Research*, *113*(F2), F02019. https://doi.org/10.1029/2006jf000745

Laraque, A., Guyot, J. L., & Filizola, N. (2009). Mixing processes in the Amazon River at the confluences of the Negro and Solimnoes rivers, Encontro das Aquas, Manaus, Brasil. *Hydrological Processes*, *23*(22), 3131–3140. https://doi.org/10.1002/hyp.7388

Lewis, Q., Rhoads, B., Sukhodolov, A., & Constantinescu, G. (2020). Advective lateral transport of streamwise momentum controls mixing at small river confluences. *Water Resources Research*, *56*(9), e2019WR026817. https://doi.org/10.1029/2019WR026817

Lewis, Q. W., & Rhoads, B. (2015). Rates and patterns of thermal mixing at a small stream confluence under variable incoming flow conditions. *Hydrological Processes*, *29*(20), 4442–4456. https://doi.org/10.1002/hyp10496

Li, K., Tang, H., Yuan, S., Xu, L., Xiao, Y., & Gualtieri, C. (2022). Temporal variations of sediment and morphological characteristics at a large confluence accounting for the effects of floodplain submergence. *International Journal of Sediment Research*, *37*(5), 619–638. https://doi.org/10.1016/j.ijsrc.2022.04.004

Li, K., Tang, H., Yuan, S., Xiao, Y., Xu, L., Huang, S., et al. (2022). A field study of near-junction-apex flow at a large river confluence and its response to the effects of floodplain flow. *Journal of Hydrology*, *610*, 127983. https://doi.org/10.1016/j.jhydrol.2022.127983

Lyubimova, T., Lepikhin, A., Konovalov, V., Parshakova, Y., & Tiunov, A. (2014). Formation of the density currents in the zone of confluence of two rivers. *Journal of Hydrology*, *508*, 328–342. https://doi.org/10.1016/j.jhydrol.2013.10.041

Lyubimova, T. P., Lepikhin, A. P., Parshakova, Y. N., Kolchanov, V. Y., Gualtieri, C., Roux, B., & Lane, S. N. (2020). A numerical study of the influence of channel-scale secondary circulation on mixing processes downstream of river junctions. *Water*, *12*(11), 2969. https://doi.org/10.3390/w12112969

Marinho, T., Furtado, A., Dos Santos, V., Zumak, A., Nascimento, A., & Filizola, N. (2022). Riverbed morphology and hydrodynamics in the confluence of complex mega rivers - A study in the Branco and Negro rivers, Amazon basin. *Journal of South American Earth Sciences*, *118*, 103969. https://doi.org/10.1016/j.jsames.2022.103969

Martí-Cardona, B., Arbat-Bofill, M., Prats, J., & Pipia, L. (2016). Thermal remote sensing for reservoir modelling and management. In *Living Planet Symposium, May 2016, Prague, Czech Republic. SP-740*.

Martone, I., Gualtieri, C., & Endreny, T. A. (2020). Characterization of hyporheic exchange drivers and patterns within a Low-gradient, first-order, river confluence during low and high flow. *Water*, *12*(3), 649. https://doi.org/10.3390/w12030649

Mohsen, A., Kovács, F., Mezősi, G., & Kiss, T. (2021). Sediment transport dynamism in the confluence area of two rivers transporting mainly suspended sediment based on Sentinel-2 satellite images. *Water*, *13*(21), 3132. https://doi.org/10.3390/w13213132

Mosley, M. P. (1976). An experimental study of channel confluences. *The Journal of Geology*, *84*(5), 535–562. https://doi.org/10.1086/628230

Nordin, C. F., Meade, R. H., Mahoney, H. A., & Delaney, B. M. (1977). Particle size of sediments collected from the bed of the Amazon River and its tributaries in June and July 1976. In *USGS open file−report 77−400, Denver, USA*.

Park, E., & Latrubesse, E. M. (2015). Surface water types and sediment distribution patterns at the confluence of mega rivers: The Solimoes-Amazon and Negro Rivers junction. *Water Resources Research*, *51*(8), 6197–6213. https://doi.org/10.1002/2014wr016757

Parsons, D. R., Best, J. L., Lane, S. N., Orfeo, O., Hardy, R. J., & Kostaschuk, R. (2007). Form roughness and the absence of secondary flow in a large confluence–diffluence, Rio Parana, Argentina. *Earth Surface Processes and Landforms*, *32*(1), 155–162. https://doi.org/10.1002/esp.1457

Plesniak, M. W., Mehta, R. D., & Johnston, J. P. (1996). Curved two-stream turbulent mixing layers revisited. *Experimental Thermal and Fluid Science*, *13*(3), 190–205. https://doi.org/10.1016/s0894-1777(96)00080-5

Pouchoulin, S., Le Coz, J., Mignot, E., Gond, L., & Riviere, N. (2020). Predicting transverse mixing efficiency downstream of a river confluence. *Water Resources Research*, *56*(10), e2019WR026367. https://doi.org/10.1029/2019WR026367

Prats, J., Armengol, J., Marcé, R., Sánchez-Juny, M., & Dolz, J. (2010). Dams and reservoirs in the lower Ebro River and its effects on the river thermal cycle. *Hdb. Envion. Chem.*, *13*, 77–95.

Ramón, C. L., Armengol, J., Dolz, J., Prats, J., & Rueda, F. (2014). Mixing dynamics at the confluence of two large rivers undergoing weak density variations. *J. Geophys. Res.-Oceans*, *119*(4), 2386–2402. https://doi.org/10.1002/2013jc009488

Ramón, C. L., Hoyer, A. B., Armengol, J., Dolz, J., & Rueda, F. J. (2013). Mixing and circulation at the confluence of two rivers entering a meandering reservoir. *Water Resources Research*, *49*(3), 1429–1445. https://doi.org/10.1002/wrcr.20131

Rhoads, B., & Sukhodolov, A. (2001). Field investigation of three dimensional flow structure at stream confluences: 1. Thermal mixing and time-averaged velocities. *Water Resources Research*, *37*(9), 2393–2410.

Rice, S. P., Kiffney, P., Greene, C., & Pess, G. R. (2008). Confluences, tributaries and the fluvial network. In S. P. Rice, A. G. Roy, & B. Rhoads (Eds.), *The ecological importance of tributaries and confluences, river confluences, tributaries and the fluvial network* (pp. 17–32). Wiley & Sons.

Riley, J. D., Rhoads, B., Parsons, D. R., & Johnson, K. K. (2014). Influence of junction angle on three-dimensional flow structure and bed morphology at confluent meander bends during different hydrological conditions. *Earth Surface Processes and Landforms*, *40*(2), 252–271. https://doi.org/10.1002/esp.3624

Rodi, W., Constantinescu, G., & Stoesser, T. (2013). *Large eddy simulation in hydraulics IAHR monograph*. CRC Press, Taylor & Francis Group.

Shen, X., Hodges, B., Li, R., Li, Z., Fan, J., Cui, N., & Cai, H. (2021). Factors influencing distribution characteristics of total dissolved gas supersaturation at confluences. *Water Resources Research*. https://doi.org/10.1029/2020R028760

Sime, L., Ferguson, R., & Church, M. (2007). Estimating shear stress from moving boat acoustic Doppler measurements in a large gravel bed river. *Water Resources Research*, *43*(12), W03418. https://doi.org/10.1029/2006WR005069

Souza de Morais, E., dos Santos, M. L., Cremon, E. H., & Stevaux, J. C. (2016). Floodplain evolution in a confluence zone: Paraná and Ivaí rivers, Brazil. *Geomorphology*, *257*, 1–9. https://doi.org/10.1016/j.geomorph.2015.12.017

Spalart, P. R. (2009). Detached-eddy simulation. *Annual Review of Fluid Mechanics*, *41*(1), 181–202. https://doi.org/10.1146/annurev.fluid.010908.165130

Sukhodolov, A. N., & Rhoads, B. (2001). Field investigation of three-dimensional flow structure at stream confluences: 2. Turbulence. *Water Resources Research*, *37*(9), 2411–2424. https://doi.org/10.1029/2001wr000317

Sukhodolov, A. N., Shumilova, O. O., Constantinescu, G. S., Lewis, Q., & Rhoads, B. L. (2023). Mixing at river confluences governed by intermodal behavior. *Nature Geoscience*, *16*(1), 89–93. https://doi.org/10.1038/s41561-022-01091-1

Sukhodolov, A. N., & Sukhodolova, T. A. (2019). Dynamics of flow at concordant gravel bed river confluences: Effects of junction angle and momentum flux ratio. *Journal of Geophysical Research: Earth Surface*, *124*(2), 588–615. https://doi.org/10.1029/2018JF004648

Szupiany, R. N., Amsler, M. L., Parsons, D. R., & Best, J. L. (2009). Morphology, flow structure, and suspended bed sediment transport at two large braid-bar confluences. *Water Resources Research*, *45*(5). https://doi.org/10.1029/2008WR007428

Trevethan, M., Martinelli, A., Oliveira, M., Ianniruberto, M., & Gualtieri, C. (2015). Fluid dynamics sediment transport and mixing about the confluence of Negro and Solimões rivers, Manaus Brazil. In *36th IAHR World Congress, the Hague, the Netherlands, June 28–July 3 paper no. 80094*.

Umar, M., Rhoads, B., & Greenberg, J. A. (2018). Use of multispectral satellite remote sensing to assess mixing of suspended sediment downstream of large river confluences. *Journal of Hydrology*, *556*, 325–338. https://doi.org/10.1016/j.jhydrol.2017.11.026

Xu, L., Yuan, S., Tang, H., Qiu, J., Xiao, Y., Whittaker, C., & Gualtieri, C. (2022). Mixing dynamics at the large confluence between the Yangtze River and Poyang Lake. *Water Resources Research*, *58*(11), e2022WR032195. https://doi.org/10.1029/2022WR032195

Yuan, S., Lin, J., Tang, H., Zhu, Y., Ran, Q., Constantinescu, G., & Gualtieri, C. (2024). Near-surface turbulent dissipation at a laboratory-scale confluence: Implications on gas transfer. *Environmental Fluid Mechanics*, *24*(6), 1099–1122. https://doi.org/10.1007/s10652-023-09964-8

Yuan, S., Qiu, J., Tang, H., Xu, L., Xiao, Y., Liu, M., et al. (2023). Fish community traits near a large confluence: Implications for its nodal effects in the river ecosystem. *Journal of Hydrology*, *626*, 130335. https://doi.org/10.1016/j.jhydrol.2023.130335

Yuan, S., Tang, H., Li, K., Xu, L., Xiao, Y., Gualtieri, C., et al. (2021). Hydrodynamics, sediment transport and morphological features at the confluence between the Yangtze River and the Poyang Lake. *Water Resources Research*, *57*(3), e2020WR028284. https://doi.org/10.1029/2020WR028284

Yuan, S., Xu, L., Tang, H., Xiao, Y., & Gualtieri, C. (2022). The dynamics of river confluences and their effects on the ecology of aquatic environment: A review. *Journal of Hydrodynamics*, *34*, 1–14. https://doi.org/10.1007/s42241-022-0001-z

Yuan, S., Yan, G., Tang, H., Xiao, Y., Rahimi, H., Aye, N., & Gualtieri, C. (2023). Effects of tributary floodplain on confluence hydrodynamics. *Journal of Hydraulic Research*, *61*(4), 552–572. https://doi.org/10.1080/00221686.2023.2231413

Yuan, S., Zheng, Y., Tang, H., Chen, Y., Xu, L., Whittaker, C., & Gualtieri, C. (2024). Large wood transport and accumulation near the separation zone of a channel confluence. *Water Resources Research*, *60*(3), e2023WR034790. https://doi.org/10.1029/2023WR034790

Zeng, J., Constantinescu, G., Blanckaert, K., & Weber, L. (2008). Flow and bathymetry in sharp open-channel bends: Experiments and predictions. *Water Resources Research*, *44*(9), W09401. https://doi.org/10.1029/2007WR006303